# *Spitzer* View of Young Massive Stars in the LMC H II Complexes. II. N 159

C.-H. Rosie Chen[1], Remy Indebetouw[1,2], You-Hua Chu[3], Robert A. Gruendl[3,4], Gérard Testor[5], Fabian Heitsch[6], Jonathan P. Seale[3], Margaret Meixner[7], and Marta Sewilo[7]

## ABSTRACT

The H II complex N 159 in the Large Magellanic Cloud (LMC) is used to study massive star formation in different environments, as it contains three giant molecular clouds (GMCs) that have similar sizes and masses but exhibit different intensities of star formation. We identify candidate massive young stellar objects (YSOs) using infrared photometry, and model their SEDs to constrain mass and evolutionary state. Good fits are obtained for less evolved Type I, I/II, and II sources. Our analysis suggests that there are massive embedded YSOs in N 159B, a maser source, and several ultracompact H II regions. Massive O-type YSOs are found in GMCs N 159-E and N 159-W, which are associated with ionized gas, i.e., where massive stars formed a few Myr ago. The third GMC, N 159-S, has neither O-type YSOs nor evidence of previous massive star formation. This correlation between current and antecedent formation of massive stars suggests that energy feedback is relevant. We present evidence that N 159-W is forming YSOs spontaneously, while collapse in N 159-E may be triggered. Finally, we compare star formation rates determined from YSO counts with those from integrated H$\alpha$ and 24 $\mu$m luminosities and expected from gas surface densities. Detailed dissection of extragalactic GMCs like the one presented here is key to revealing the physics underlying commonly used star formation scaling laws.

[1]Department of Astronomy, University of Virginia, Charlottesville, VA 22903, USA

[2]National Radio Astronomical Observatory, Charlottesville, VA 22904, USA

[3]Department of Astronomy, University of Illinois, Urbana, IL 61801, USA

[4]Visiting Astronomer, Cerro Tololo Inter-American Observatory. CTIO is operated by AURA, Inc. under contract to the National Science Foundation.

[5]Observatoire de Paris, 92195 Meudon, France

[6]Department of Physics and Astronomy, University of North Carolina at Chapel Hill, Chapel Hill, NC 27599, USA

[7]Space Telescope Science Institute, Baltimore, MD 21218, USA

*Subject headings:* H II regions – infrared: stars – ISM: individual (N 159) – Magellanic Clouds – stars: formation – stars: pre-main sequence

## 1. Introduction

Despite significant progresses in understanding the physics of single star formation, we still have only crude ideas about why some giant molecular clouds (GMCs) form clusters, some form distributed associations, and some form very few stars. To make headway, key properties of GMCs displaying various intensities of star formation must be explored observationally in detail. After massive stars are formed, their energy feedback through ionizing fluxes, fast stellar winds, and supernova explosions can alter the physical conditions of a GMC, subsequently enhancing or inhibiting further star formation. If a knowledge of stellar content and energy feedback is obtained, it is then possible to assess the relative importance of self-propagating, triggered, and spontaneous star formation, and even further estimate the star formation efficiency of a GMC. It is thus crucial to inventory massive stars and young stellar objects (YSOs) associated with GMCs. The YSOs are particularly important as they provide the most direct probes for causal relationship between the initial condition (gas) and the end product (stars).

Such study is straightforward in concept, but difficult in practice because in distant galaxies the stellar content is not resolved, and in the Milky Way the distances and associations among stars and their interstellar environments are uncertain. The Large and Small Magellanic Clouds (LMC and SMC) are the only nearby star-forming galaxies in which stars are at common, known distances and can be resolved individually. Recent high-sensitivity mid-IR *Spitzer Space Telescope (SST)* observations make it possible to study a large sample of YSOs in the MCs (e.g., Whitney et al. 2008; Gruendl & Chu 2009; Simon et al. 2007). The nearly face-on orientation and thin disk structure of the LMC make it easy to identify physical associations between YSOs and their interstellar environments. All objects in the LMC can be considered to be at a uniform distance, with <10% error, of 50 kpc (Feast 1999). In our recent study of massive YSOs in the LMC H II complex N 44 (Chen et al. 2009, hereafter Paper I), we examined three GMCs with different star formation properties: the central and southern GMCs are associated with bright H II regions and have O-type YSOs, while the northern GMC contains only a few faint, small H II regions and has no O-type YSOs. The close association of massive YSOs with H II regions in GMCs suggests that massive stars preferentially form in regions where massive stars have been formed previously, within the last few Myr. It is not clear whether this result is a special case for N 44 or can be generalized.

We have thus selected more LMC H II complexes with different morphologies of ionized gas and molecular clouds to examine their YSO content and distribution. This study reports massive star formation in the H II complex LH$\alpha$ 120-N 159 (hereafter N159; Henize 1956). N 159 is located between two regions with contrasting activities: to its north are a string of active star formation regions such as 30 Doradus, N 158, and N 160, and to its south lies a large molecular ridge with little star formation activity (e.g., Indebetouw et al. 2008). The ionized gas of N 159 shows two prominent lobes in the central region, surrounded by smaller H II regions (Figure 1a). The two prominent H II lobes exhibit filamentary arcs resultant from interactions with stellar winds and a supernova remnant (SNR) in the northern lobe (Chu et al. 1997; Williams et al. 2000). The northern and southern lobes appear to be separated by dark clouds, but their independent systems of circular filaments do not suggest a common origin for their photoionization and dynamic shaping. The stellar content of N 159 has been identified loosely as an OB association, i.e., LH105 (Lucke & Hodge 1970). Based on integrated colors and association with discrete H II regions in N 159, Bica et al. (1996) identified three young clusters of ages $< 10$ Myr in the A, F, and D components, and an OB association in the C component (see Figure 1a for the identification of H II components).

Surveys of CO toward N 159 (Figure 1b) show three molecular concentrations whose peaks correspond to three GMCs, N 159-E, N 159-W, and N 159-S, respectively (Johansson et al. 1998). The similarity in their radial velocities, $V_{\rm lsr} = 234.1 - 238.5$ km s$^{-1}$, suggests that they are likely physically related. N 159-E is associated with the central prominent H II regions of N 159, the bulk of the OB association LH105 (Lucke & Hodge 1970), which include the young cluster in the D component. N 159-W, an immediate neighbor of N 159-E, hosts a few small, bright H II regions and the western part of LH105, which includes the two young clusters in the A and F components. In sharp contrast, the GMC N 159-S shows a much lower level of star formation with only a couple of very faint diffuse H II regions and no OB associations, although it is similar in size and even larger in mass compared with each of its northern neighbors at $\sim 3'$ away. A recent study by Nakajima et al. (2005) identified candidate Herbig Ae/Be (HAeBe) stars in GMC N 159-S and suggested that cluster formation had just begun in this GMC. However, it is not clear whether the scarcity in massive stars seen in the optical and near-IR wavelengths in this GMC is caused by massive stars being still at infancy and deeply embedded in circumstellar material, or not being formed actively at all.

To study the current massive star formation in N 159, we have used archival *Spitzer* mid-IR observations and obtained complementary ground-based optical and near-IR observations. These observations have been analyzed and the results are reported in this paper. Section 2 describes the observations and data reduction. Section 3 reports the identification and classification of YSO candidates. In Section 4 we determine the physical properties of the

YSOs by modeling their spectral shapes. In Section 5 we discuss the massive star formation properties. A summary is given in Section 6.

## 2. Observations and Data Reduction

We have used *Spitzer* mid-IR observations to diagnose YSOs. To extend the spectral energy distribution (SED) and to improve the angular resolution, we have further obtained ground-based optical and near-IR imaging observations of N 159. We have also retrieved available images in the *Hubble Space Telescope* (*HST*) archive to examine the optical counterparts and environments of the YSOs.

### 2.1. *Spitzer* IRAC and MIPS Observations

Archival *Spitzer* observations from the Legacy Program Surveying the Agents of a Galaxy's Evolution (SAGE; Meixner et al. 2006) and GTO Program 124 (PI: Gehrz) were used to study YSOs in N 159. These observations include images taken with the Infrared Array Camera (IRAC; Fazio et al. 2004) at 3.6, 4.5, 5.8, and 8.0 $\mu$m and the Multiband Imaging Photometer for *Spitzer* (MIPS; Rieke et al. 2004) at 24, 70, and 160 $\mu$m. The observation summary is listed in Table 1, in which the program ID, principal investigator, and typical observation parameters are given.

We have adopted the *Spitzer* photometry of point sources from Gruendl & Chu (2009). The photometric data are used to construct SEDs, and the images are used to examine the structure of cold and partially ionized interstellar matter. To cover regions associated with the three GMCs around N 159, the field we have analyzed is $12' \times 12\farcm5$ and is shown in Figure 2 in the 3.6, 8.0, and 24 $\mu$m bands. The 3.6 $\mu$m image is dominated by stellar emission, the 8.0 $\mu$m image shows the polycyclic aromatic hydrocarbon (PAH) emission, and the 24 $\mu$m image is dominated by dust continuum emission (Li & Draine 2001, 2002; Draine & Li 2007). To better illustrate the relative distribution of emission in different bands, we have produced a color composite with 3.6, 8.0, and 24 $\mu$m images mapped in blue, green, and red, respectively. In this color composite (Figure 2d), dust emission appears red and diffuse, stars appear as blue point sources, red supergiants appear yellow, and dust-shrouded YSOs and evolved stars appear red.

### 2.2. CTIO 4 m ISPI Observations

We obtained near-IR images in the $J$ and $K_s$ bands with the Infrared Side Port Imager (ISPI; van der Bliek et al. 2004) on the Blanco 4 m telescope at Cerro Tololo Inter-American Observatory (CTIO) on 2006 November 9. The images were obtained with the 2K × 2K HgCdTe HAWAII-2 array, which had a pixel scale of $0\farcs3$ pixel$^{-1}$ and a field-of-view of $10\farcm25 \times 10\farcm25$. N 159 was observed in one field with ten 30 s exposures in the $J$ band and twenty 30 s exposures in the $K_s$ band (each of the latter was coadded from two 15 s frames to avoid background saturation). The observations were dithered to aid in the removal of transients and chip defects. The sky observations were made before and after each set of ten on-source exposures. All images were processed using the IRAF package `cirred` for dark and sky subtraction and flat-fielding. The astrometry of individual processed images was solved with the routine `imwcs` in the package `wcstools`. The astrometrically calibrated images are then coadded to produce a total exposure map for each filter. The flux calibration was carried out using 2MASS photometry of isolated sources.

As some of the YSOs appear extended in the ISPI images, we have used additional $J$ and $K_s$ images taken with the Nasmyth Adaptive Optics System and Near-Infrared Imager and Spectrograph (NACO) on the 8.2 m Very Large Telescope (VLT) at the European Southern Observatory (ESO) (Testor et al. 2006, 2007). These images have a pixel size of $0\farcs027$-$0\farcs054$ pixel$^{-1}$ and a superb resolution of $0\farcs11$-$0\farcs25$, and are thus used to resolve compact groups of YSOs.

### 2.3. Archival *HST* Images

We have searched the *HST* archive for Wide Field Planetary Camera 2 (WFPC2) and Advanced Camera for Surveys (ACS) images in the field of N 159. These observations are listed in Table 2, in which the coordinate, program ID, PI, detector, filter, and total exposure time are given. Each observation contains multiple exposures for the same pointing and filter, and these images have been pipeline-processed to remove cosmic rays and to produce a total exposure map, which is available in the Hubble Legacy Archive[1].

Four fields have observations, but not all are useful; for example, the wide $U$ band

[1]Based on observations made with the NASA/ESA Hubble Space Telescope, and obtained from the Hubble Legacy Archive, which is a collaboration between the Space Telescope Science Institute (STScI/NASA), the Space Telescope European Coordinating Facility (ST-ECF/ESA) and the Canadian Astronomy Data Centre (CADC/NRC/CSA).

(F300W) images have very low S/N. The most useful images are those taken with the H$\alpha$ filter (WFPC2/F656N or ACS/F658N) or broad-band filters at longer wavelengths such as Strömgren $y$ (F547M) or WFPC2 $VI$ (F555W and F814W). The former show ionized gas and the latter show stars at high resolution.

### 2.4. Other Available Datasets

To construct SEDs for sources in the *Spitzer* catalog from Gruendl & Chu (2009), we have expanded the catalog by adding optical $UBVI$ photometry from the Magellanic Cloud Photometric Survey (MCPS; Zaritsky et al. 2004) and near-IR $JHK_s$ photometry from the Point Source Catalog of the Two Micron All Sky Survey (2MASS; Skrutskie et al. 2006). As the 2MASS catalog is relatively shallow with a photometric limit of $K_s \sim 14.5$, we have also used the point source catalog from the InfraRed Survey Facility (IRSF; Kato et al. 2007), which is $\sim$ 2 mag deeper than the 2MASS catalog, to match the IRAC sources that do not have 2MASS counterparts. When merging the datasets, we allow a $1''$ error margin for matching *Spitzer* sources with optical or near-IR sources. Thus, for each *Spitzer* source, the magnitudes from $U$ to 70 $\mu$m can be converted to flux densities using the corresponding zero-magnitude flux listed in Table 3 and then used to construct the SED.

We have used H$\alpha$ images of N 159 from the Magellanic Cloud Emission-Line Survey (MCELS; Smith & The MCELS Team 1999) to examine the large-scale distribution of dense ionized gas and to compare with images at other wavelengths. As the angular resolution of this survey is $\sim 2''$, we have used additional H$\alpha$ images taken with the MOSAIC camera on the CTIO Blanco 4 m telescope that cover the northern part of our working field (Seward et al. 2010). These images, with a pixel size of $0\farcs27$ pixel$^{-1}$, are used to show the immediate environments of YSOs. Finally, as stars are formed from molecular gas, we have also used the CO observations from the Magellanic Mopra Assessment (MAGMA; Ott et al. 2008; Hughes et al. 2010) to examine the distribution of molecular clouds in N 159.

## 3. Identification of Massive YSOs

### 3.1. Selection of Massive YSO Candidates

YSOs are enshrouded in dust that absorbs stellar UV and optical radiation and re-radiates in the IR. Thus, YSOs can be distinguished from normal stars, i.e., main-sequence, giant, and supergiant stars, from their excess IR emission; they are positioned in redder parts of the color-color and color-magnitude diagrams (CMDs) than normal stars. However,

background galaxies and evolved stars such as asymptotic giant branch (AGB) stars can also be red sources, and these contaminants exist in non-negligible numbers. In Paper I and Gruendl & Chu (2009), we have demonstrated that using two color-magnitude criteria $([4.5]-[8.0]) \geq 2.0$ and $[8.0] < 14-([4.5]-[8.0])$, galaxies and evolved stars can be effectively excluded for the initial selection of massive YSOs. We have thus applied the same criteria to select YSO candidates in N 159. Note that although the full LMC catalogs of YSO candidates have been constructed using similar methods (Whitney et al. 2008; Gruendl & Chu 2009), as will be discussed in §3.4, a detailed analysis on small regions together with new information such as deep near-IR photometry as we perform here will be more complete and also useful in diagnosing sources that might have been previously mis-identified.

Figure 3a displays the [8.0] versus ([4.5]−[8.0]) CMD of all sources detected in N 159. To illustrate the locations of AGB stars in the CMD, models for Galactic C- and O-rich AGB stars (Groenewegen 2006) are also plotted. Although the LMC metallicity is only 1/3 solar, as confirmed in Blum et al. (2006), these Galactic models should be good approximations for LMC objects since the chemistry of AGB atmospheres is dominated by nucleosynthesized material. To avoid crowding, we plot only models for a stellar luminosity of 3000 $L_{\odot}$ to illustrate the range of colors. For a luminosity range $1 \times 10^3 - 6 \times 10^4 L_{\odot}$ (Pottasch 1993), the expected loci of AGB stars in the CMD can move vertically from 1.2 to −3.3 mag. We have also searched the known evolved stars in N 159 in the SIMBAD database and found 4 confirmed AGB stars at various evolutionary stages: 2 carbon stars and 2 OH/IR stars. These 4 objects are marked with open squares in the [8.0] versus ([4.5]−[8.0]) CMD (Figure 3a). Their locations overlap with AGB stellar models and our selection criteria indeed exclude them.

We obtain a list of 52 YSO candidates from the above selection criteria, however, they still include a significant number of small dust knots, obscured evolved stars, and bright background galaxies. These contaminants need to be examined closely to assess their nature and to be excluded from the YSO list. Following the procedures outlined in Paper I, to better resolve these IR sources and their environments, we examine the *HST*, CTIO 4m ISPI $JK_s$, and CTIO 4m MOSAIC H$\alpha$ images. We further use the multi-wavelength catalog described in §2.4 to construct SEDs from the $U$-band to 70 $\mu$m. Using these images and SED data, we have assessed whether the candidates are truly YSOs.

### 3.2. Identification of Contaminants

Background galaxies can be identified from their morphologies if they are resolved. Two of our CMD-selected YSO candidates, sources 054037.09−694521.5 and 054044.66−694550.9

show elongated, extended emission around the point sources in high-resolution MOSAIC and ISPI images. The SEDs of these two sources are similar to those of late-type galaxies, i.e., characterized by two broad humps, one from stellar emission over optical and near-IR wavelength range and the other from dust emission over mid- to far-IR range. In addition, the interstellar environment around these two sources are relatively dust free as they have little diffuse 8 $\mu$m emission in the surroundings. Based on these considerations, these two CMD-selected YSO candidates are reclassified as background galaxies.

Warm interstellar dust may show mid-IR SEDs indicative of PAH emission (e.g., Gorjian et al. 2004), similar to those of circumstellar dust in YSOs. As the angular resolution of IRAC images is $\sim 2''$, corresponding to 0.5 pc for a LMC distance of 50 kpc, some small dust clumps may be identified as point sources and included in the YSO candidate list. In addition, a main-sequence star projected near a dust clump or superposed on dust filaments may also make its way into our YSO candidate list. To identify these two types of YSO imposters, we use our high angular resolution ($0\farcs3$ pixel$^{-1}$) ISPI $JK_s$ images. In the ISPI images, stars or YSOs appear unresolved and can be further differentiated with the $J - K_s$ color as stars are brighter in $J$ and YSOs brighter in $K_s$. Dust clumps may appear as extended emission or have no point-like counterparts in the ISPI $K_s$ image. These dust clumps are unlikely to have highly embedded massive YSOs since none of them have bright 24 $\mu$m point sources as would have been expected for such YSOs; however, they may have YSOs with lower masses. As a reference, Herbig Ae stars of A0-type at different evolutionary stages would have been detected, because AB Aur and Lk H$\alpha$ 25 (Hillenbrand et al. 1992) placed at the LMC distance would have $K_s = 16.9$ and 18.6, respectively, and the photometric limit of our $K_s$ images at 10-$\sigma$ level is $\sim 17.6$ mag and the 3-$\sigma$ detection limit is $\lesssim 19.0$ mag (Gruendl & Chu 2009). Aided by the ISPI images, we find that 16 of our 52 YSO candidates are interstellar dust clumps, and another 7 are stars projected near dust clumps.

### 3.3. Massive YSOs and Their Classification

The results of our examination of 52 YSO candidates are given in Table 4, which lists source name, ranking of the brightness at 8 $\mu$m, magnitudes in the 3.6, 4.5, 5.8, 8.0, 24, and 70 $\mu$m bands, source classification, and remarks. Each source's magnitudes in the $U$, $B$, $V$, $I$, $J$, $H$, $K_s$ bands are given in Table 5. Note that some of the YSOs appear as single sources in IRAC images but are resolved into multiple sources in high-resolution ISPI and VLT/NACO images; for these sources, the photometric measurements in Table 5 were made for the dominant YSO sources, i.e., the brightest $K_s$ sources with the reddest $J - K_s$ colors. The "Flag" in Table 5 gives the origin of data from which $JHK_s$ are measured. The results

of YSO identification are shown in the [8.0] versus ([4.5]−[8.0]) CMD (Figure 3b). Among the 52 YSO candidates, we identified 2 background galaxies, 16 dust clumps, and 7 stars superposed on dust. After excluding these sources, 27 YSO candidates remain. As these are most likely bona fide YSOs, we will simply call them YSOs in the rest of the paper.

Following the classification scheme proposed in Paper I, we have further categorized these YSOs into Type I, II, and III by analyzing their properties and corresponding SED plots. Type I YSOs have SEDs with a steep rise from the near-IR to 24 $\mu$m as the radiation is mostly from their circumstellar envelopes. They are generally not visible in the optical or $J$-band, but are visible in the $K_s$-band and bright at 24-70 $\mu$m. Type I YSOs are often found in or behind dark clouds. Type II YSOs have SEDs with a low peak in the optical and a high peak at 8-24 $\mu$m corresponding to stellar core and circumstellar disk, respectively, after the envelope has dissipated. Type II YSOs are faint in the optical, but bright in the $J$-band to 8 $\mu$m, and then faint again at the 24 $\mu$m. Type III YSOs have SEDs peaking in the optical with a modest amount of dust emission in the near- to mid-IR as they are largely exposed but still possess remnant circumstellar material. Their brightness fades in the longer wavelength and they are often surrounded by H II regions. The results of our classification of 27 YSOs are also given in Table 4. Multi-wavelength images and SEDs of these YSOs have been shown in Gruendl & Chu (2009), though differences exist in some SEDs between theirs and this study due to the inclusion of aforementioned deeper near-IR catalogs and that 24 $\mu$m upper limits were estimated for a few YSOs in order to better constrain model fitting to these SEDs as discussed later in §4.

### 3.4. Comparison with YSO Samples Identified by Others

N 159 contains the first extragalactic protostar discovered by Gatley et al. (1981) using ground-based near- to mid-IR $JHKL'$ photometry; this protostar corresponds to our YSO 053959.34−694526.3. Using sensitive *Spitzer* observations, more YSOs in N 159 have been identified using various methods by Jones et al. (2005), Whitney et al. (2008), and Gruendl & Chu (2009). Gruendl & Chu (2009) used the same *Spitzer* data and selection criteria, and identified 25 YSOs. Our assessments retain two more sources in the YSO sample, 053952.60−694517.0 and 054050.85−695001.9, which were classified as a diffuse source and a background galaxy in their list. The reclassification is aided by the ISPI $JK_s$ images and IRSF $JHK_s$ photometry. For source 053952.60−694517.0 which was previously considered as (bright) stars superposed on a dust clump, the ISPI images show a faint red source ($K_s \sim 17.0$ and $J - K \sim 0.3$) resolved from nearby bright stars within the IRAC PSF. For source 054050.85−695001.9 whose SED was once composed of only a nearly flat slope

over 3.6–24 $\mu$m, the inclusion of IRSF $JHK_s$ photometry makes its SED (Figure 5) more consistent with a YSO than a galaxy.

Jones et al. (2005) identified YSO candidates by comparing source locations in the ([3.6]−[4.5]) versus ([5.8]−[8.0]) color-color diagram with those expected from low-mass YSO models (Allen et al. 2004) . They studied a smaller region centered on the prominent central H II regions, within which we find 21 YSOs while they find only five YSO candidates. In Figure 4a, we mark the locations of their five YSO candidates and our YSOs in the 8 $\mu$m image of N 159, and in Figure 4b we compare their sources with ours in the [8.0] versus ([4.5]−[8.0]) CMD. All of their five YSO candidates fall within the YSO wedge bounded by [4.5]−[8.0] $\geq$ 2.0 and [8.0] $\geq$ 14.0−([4.5]−[8.0]), and form a subset of our YSO sample. To investigate why the majority of our YSOs in N 159 are missed in their study, we further compare our sources with their photometric catalog (Tables 1 and 2 in Jones et al. 2005). We find that the discrepancy between our and their YSO lists is attributed to both different selection criteria for point sources and different criteria for YSOs. Jones et al. used stringent parameters in the automated search for point sources, discarding any source that appear irregular compared with the IRAC PSF; this omitted eight of our YSOs, including three bright sources with [8.0] $<$ 8.0. Only 13 of our 21 YSOs were identified as point sources in their catalog, and only five of these were also classified as YSOs by Jones et al. Of the remaining eight point sources, four were classified by Jones et al. as H II regions because their 8 $\mu$m images were slightly more extended than the PSF; three sources were not classified as they did not have photometric measurements in all four IRAC bands; and one was not selected as YSO because its [5.8]−[8.0] color was $\sim$ 0.2 mag bluer than those expected for Class I low-mass YSOs. However, we find the SED of this last source, 053940.78−694632.0 in Figure 5, to be consistent with those of bona fide YSOs.

The comparison with the YSO sample of Whitney et al. (2008) is not straightforward as they used a complex set of criteria. Within N 159, they found only 4 YSO candidates. These four YSO candidates are also marked in Figure 4. The differences between our and their YSOs can be summarized as the following:

1. Within the YSO wedge bounded by [4.5]−[8.0] $\geq$ 2.0 and [8.0] $\geq$ 14.0−([4.5]−[8.0]), we find 27 YSOs, while Whitney et al. (2008) find only 3 YSO candidates, a subset of our sample. To investigate why the majority of the YSOs in N 159 are missed in Whitney et al., we further compare our sources with their original catalog, i.e., the SAGE point source catalog. We find that only one missed YSO results from different selection criteria, and the rest from defining point sources and applying signal-to-noise (S/N) thresholds when making final lists in these two studies. The SAGE catalog, similar to Jones et al., used stringent parameters for the automated search for point sources and

Whitney et al. applied a high S/N threshold to select YSO candidates. The former discards any irregular point sources compared to IRAC PSFs, resulting in only 14 of our 27 YSOs retaining in the SAGE catalog. The latter tends to exclude sources near bright neighbors or over bright background, since varying backgrounds (Figure 4a) raises photometric uncertainties and the SAGE pipeline reports conservative S/N ratios. The S/N ratios are further reduced by applying additional 10% and 30% uncertainties respectively to 5.8 and 8.0 $\mu$m measurements (Whitney et al. 2008), resulting in only 4 of the 14 sources being included in their list of YSO candidates. One of these 4 sources does not match their set of selection criteria and hence is not included as a YSO in the Whitney et al. (2008) catalog. However, the SED of this source, 054000.69−694713.4 in Figure 5, is consistent with bona fide YSOs.

2. One YSO candidate, W991 (SSTISAGE1CJ053945.37−694802.3), of the Whitney et al. sample was rejected by our more restrictive color-magnitude criteria for YSO selection that are intended to increase reliability though at the expense of missing some of the more evolved YSOs.

The photometric extraction method used for this work (from Gruendl & Chu 2009) and Paper I has allowed the inclusion of marginally extended sources and sources amid a complex interstellar background in our initial photometric catalog. Considering that $1''$ =0.25 pc in the LMC, it is often inevitable that within the IRAC PSF a YSO is blended with circumstellar outflows or interstellar features. Furthermore, YSOs in multiple systems or YSOs in ultracompact or compact H II regions (see §4.2.2 for a detailed discussion) are likely to be measured as a single source. While it is necessary to relax the search criteria for point sources in the LMC to obtain the most complete census of YSOs possible, the relaxed search also requires that individual sources are examined carefully in order to remove diffuse sources or local peaks in the dusty interstellar medium.

The color criteria commonly used for identifying low-mass YSOs, as applied in Jones et al. (2005), are too stringent for massive YSOs, particularly when they are at early evolutionary stages. As shown in models of massive YSOs, such emission is dominated by massive envelopes and hence SEDs peak toward wavelengths longer than 24 $\mu$m. These SEDs have a generally rising slope at shorter wavelengths such as IRAC bands of 3.6–8.0 $\mu$m, but show structures depending on, e.g., the detailed geometry of the dust distribution (Whitney et al. 2004). The YSO selection method used in our study should make our YSO list relatively complete for the region of the [8.0] vs. ([4.5]−[8.0]) CMD analyzed. It will however miss sources outside this region, i.e., the less embedded, more evolved, or less massive ($\lesssim 4M_{\odot}$) YSOs, as discussed in Paper I. The Whitney et al. (2008) analysis covers bluer and fainter regions in the [8.0] vs. ([4.5]−[8.0]) CMD, and thus may find YSOs that we have not analyzed,

but confusion from evolved stars and background galaxies in these regions is more severe and careful consideration of complementary information is needed to distinguish between YSOs and contaminants.

## 4. Determining YSO Properties from Model Fits of SEDs

### 4.1. Modeling the SEDs

The observed SED of a YSO can be compared with model SEDs, and the best-fit models selected by $\chi^2$ statistics can be used to infer the probable ranges of physical parameters for the YSO. We use a grid of dust radiative transfer models calculated with the HOCHUNK Monte-Carlo code (Whitney et al. 2003), each containing a point source photospheric emitter (pre-main-sequence or main-sequence spectrum), a flared circumstellar disk, a flattened rotating envelope, and a bipolar cavity (see Robitaille et al. 2006, for details). The fitting can be carried out with the fitting tool Online SED Fitter[2] (Robitaille et al. 2007). The input parameters of the SED fitter include the fluxes of a YSO and uncertainties of the fluxes. The uncertainty of a flux has two origins: the measurement itself and the absolute flux calibration. The fluxes and their measurement errors are given in Tables 4 and 5. The calibration errors are 10% in $U$, 5% in $B$, $V$, 10% in $I$, $J$, $H$, $K_s$, 5% in 3.6, 4.5, 5.8, and 8.0 $\mu$m, 10% in 24 $\mu$m, and 20% in 70 $\mu$m (Zaritsky et al. 2004; Skrutskie et al. 2006; Kato et al. 2007; IRAC Data Handbook; MIPS Data Handbook). The total uncertainty of a flux is thus the quadratic sum of the measurement error and the calibration error. We have used the above SED fitting tool to analyze the 27 YSOs in our sample. 22 of them appear single or are clearly the dominant source within the IRAC PSF, making comparisons with single-YSO models plausible. The remaining five either have no dominant YSOs or contain luminous non-YSO sources such as background stars or dust clumps within the IRAC PSF, making single-YSO models suspect. Although the total luminosities from well-reproduced SED fits to these five YSOs should still be good approximations, given the complicated nature, they are not discussed further in detailed comparisons with models.

The best-fit and acceptable SED models of the 27 YSOs are shown in Figure 5, in which the 22 "single" YSOs are arranged in the order of Types I, I/II, II, II/III, and III from our empirical classification, and within each type by order of increasing [8.0] magnitude, and the 5 "multiple" YSOs are arranged by order of increasing [8.0] magnitude. In each panel, data points are plotted in filled circles and upper limits are plotted in filled triangles; error bars

[2]The Online SED Fitter is available at http://caravan.astro.wisc.edu/protostars/sedfitter.php.

are plotted but they are usually smaller than the plot symbols. The best-fit models, with minimum $\chi^2$ ($\chi^2_{\rm min}$, see Robitaille et al. 2007, for definitions of $\chi^2$), is shown in solid black line, and the radiation from the stellar core reddened by the best-fit foreground extinction $A_V$ is shown in dashed black line. For most YSOs, their SEDs can be fitted similarly well by a range of models. We have used a cutoff of $\chi^2 - \chi^2_{\rm min} \leq 3$ for acceptable models and they are plotted in gray lines.

The results of the SED model fits are given in Table 6, where the YSOs are listed in the same order as Figure 5. The source name, [8.0] magnitude, and type from our empirical classification are listed on the left of the table, and selected physical parameters of the best-fit models are listed to the right, i.e., the stellar parameters in mass, temperature, and radius ($M_\star$, $T_\star$, and $R_\star$), envelope accretion rate ($\dot{M}_{\rm env}$), disk mass ($M_{\rm disk}$), $A_V$, and total luminosity ($L_{\rm tot}$). In addition to the parameters of the best-fit model, we have also used the acceptable models to show a possible range of stellar mass and total luminosity. We calculated weighted average $\bar{M}_\star$ and $\bar{L}_{\rm tot}$ using the $\chi^2$ values as weights, and defined the uncertainty to be the weighted standard deviation $\Delta M_\star$ and $\Delta L_{\rm tot}$ of the accepted models. For each accepted model, we have also calculated the evolutionary stage using $\dot{M}_{\rm env}/M_\star$ and $M_{\rm disk}/M_\star$ ratios as defined in Robitaille et al. (2006), i.e., $\dot{M}_{\rm env}/M_\star > 10^{-6}$ yr$^{-1}$ for Stage I sources, $\dot{M}_{\rm env}/M_\star < 10^{-6}$ yr$^{-1}$ and $M_{\rm disk}/M_\star > 10^{-6}$ for Stage II sources, and $\dot{M}_{\rm env}/M_\star < 10^{-6}$ yr$^{-1}$ and $M_{\rm disk}/M_\star < 10^{-6}$ for Stage III sources. We then calculated the range of evolutionary stage, Stage Range, with the same weighted scheme for average and standard deviation. These ranges of stellar mass, total luminosity, and evolutionary stage are also given in Table 6. Among these three quantities, total luminosity is most robust. Mass depends on pre-main-sequence evolutionary tracks, which may introduce a sysmtematic offset, and although the mass of warm circumstellar dust is relatively robust, its translation into an accretion rate and evolutionary state depends on the applicability of the single-YSO dust geometry used in our radiative transfer models.

The SED fits of the 22 "single" YSOs, as displayed in Figure 5, show different degrees of goodness-of-fit among our empirically defined YSO types. The 18 Type I, I/II, and II YSOs show good agreement between model and observed SEDs, though a number of them demonstrate that the observed fluxes are systematically lower than the modeled ones at 4.5 $\mu$m. Among the four Type III YSOs analyzed, two of them show reasonable agreement in the SED fits, while the other two exhibit significant discrepancies between models and observed SEDs. The above-mentioned discrepancies and possible causes are discussed below in §4.2.

## 4.2. Significant Discrepancies Between Model and Observed SEDs

### *4.2.1. PAH Emission in Massive YSOs*

A number of YSOs in N 159 show a brightness dip at 4.5 $\mu$m in their SEDs (Figure 5). This is similar to YSOs in Paper I, and has been suggested that the apparent dip is not an absorption feature but caused by raised fluxes from PAH emission at 3.3, 6.2, 7.7, and 8.6 $\mu$m in the other three IRAC bands, and the difference between observed and modeled SEDs is due to models not including PAHs or small grains. The existence of PAH emission in massive YSOs in the LMC has been confirmed in a recent study using *Spitzer* InfraRed Spectrometer (IRS) observations (Seale et al. 2009). Furthermore, PAH emission appears to almost ubiquitously present among massive YSOs, as it is detected in 87% of 277 IRS spectra of massive YSOs. We examined the IRS spectra of Seale et al. (2009) and found that 28 of 29 YSOs in N 44 (Paper I) and 11 of the 11 YSOs in N 159 show PAH emission in their IRS spectra, confirming our explanation of the 4.5 $\mu$m dip in SEDs as a result of PAH emission in the other three IRAC bands.

While including PAHs and small grains in YSO models is in progress (e.g., Wood et al. 2008), we can use IRS spectra to estimate the uncertainty in deriving physical parameters of YSOs with current models. We have selected YSO 053935.99−694604.1 for illustration since this source is bright enough to ensure accurate photometric measurements and its SED shows an obvious dip at 4.5 $\mu$m. Furthermore, this YSO has no silicate absorption at 10 $\mu$m in the IRS spectrum (Seale et al. 2009) so that the contribution of PAH emission can be estimated by direct comparison between photometric data and the spectrum. The photometric SED and IRS spectrum of YSO 053935.99−694604.1 are shown in Figure 6a, where PAH emission at 6.2, 7.7, 8.6 and 11.3 $\mu$m are marked. Although 4.5 $\mu$m is outside of IRS's spectral range, this photometric datapoint appears to be consistent with the continuum level extending from those around 10 and 15 $\mu$m. We thus assumed that the difference between the photometric datapoints at 5.8 and 8.0 $\mu$m and the underlying continuum level is entirely due to PAH emission and derived a factor of 1.8 for the (PAH+continuum)/continuum ratio. We divided the observed fluxes at 3.6, 5.8, and 8.0 $\mu$m by this factor and modeled the PAH-corrected SED. The model fits to the YSO's SED before and after the PAH correction is shown in Figures 6b and c; the PAH-corrected SED is well reproduced by YSO models.

The results of the fits are listed in Table 7, including $\chi^2$-weighted average and standard deviation of stellar mass, total luminosity, envelope accretion rate, and Stage Range. All four but one parameter inferred from fits to SEDs before and after PAH correction are in good agreement. The exception is $\dot{M}_{\rm env}$, whose value is larger before the PAH correction; however, this parameter is poorly constrained. This result is understandable since the raised

fluxes from PAH emission in the three IRAC bands is compensated by additional amount of larger dust grains incorporated in the models and hence the larger $\dot{M}_{\rm env}$, and the ambiguous geometry of dust distribution (in disk or envelope) causes the large uncertainties in $\dot{M}_{\rm env}$. Nonetheless, the other three main parameters are not sensitive to this contamination and thus the conclusions based on stellar mass, total luminosity, and Stage Range derived from model fits to observed SEDs without PAH corrections are not compromised.

#### *4.2.2. Discrepancies in Type III YSOs*

Among the four Type III YSOs, two show significant discrepancies between the best-fit models and the observed SEDs: 053945.18−694450.4 and 054004.40−694437.6 (Figure 5). These two YSOs have SEDs agreeing with the stellar photospheric emission in near-IR but deviant in optical bands. To understand the cause of this discrepancy, we examine available high-resolution optical images, i.e., the 4m MOSAIC H$\alpha$ and archival *HST* images. These images show that both YSOs have already formed compact H II regions. YSO 053945.18−694450.4 has a small H II region of diameter $\sim 4\farcs8$ (=1.2 pc), resolved in the MOSAIC H$\alpha$ image. YSO 054004.40−694437.6 coincides with the compact H II region the Papillon Nebula (Heydari-Malayeri et al. 1999) of diameters $\sim 4\farcs4 \times 2\farcs8$ (= 1.1pc × 0.7 pc), resolved in both MOSAIC and *HST* images.

For both YSOs, the optical $UBVI$ photometry were adopted from MCPS catalog. This catalog used broad-band images taken with a CCD camera of a $0\farcs7$ pixel$^{-1}$ scale and under seeings of $1\farcs2$-$1\farcs8$ (Zaritsky et al. 2004). Thus, compact H II regions of radii $\lesssim 2''$ are unlikely to be resolved from the central stars. Bright nebular emission lines such as H$\beta$ would have significant contribution to $B$ and $V$ bands, and hence these fluxes deviate from stellar models, resulting in larger uncertainties in physical parameters inferred from SED fits. Furthermore, the presence of H II regions also suggests that the dust emission can have an interstellar, instead of circumstellar, origin. Thus, the inferred envelope accretion rate and disk mass are less reliable, and so is the Stage. This is similar to the YSO associated with a small H II region resolved by *HST* in N44, YSO 052207.3−675819.9 (Paper I). These results signify the importance of using high-resolution H$\alpha$ images to reveal small H II regions that are responsible for the dust emission and indicate the last evolutionary stage as a YSO approaches the main sequence stage. On the other hand, the good agreement among mass estimates for YSO 052207.3−675819.9 using different independent methods demonstrates that for a SED relatively well reproduced by models (and hence a good estimate for the total luminosity of the system), the mass of the central star inferred from SED fits remains reliable. This is likely the case for YSO 053945.18−694450.4. As for YSO 054004.40−694437.6, the

system is more complicated and will be discussed in §4.3.

### 4.3. Multiplicity Effect on SED Fits – Modeling a Group of YSOs

At the LMC's distance of 50 kpc, IRAC's $\sim 2\farcs0$ angular resolution translates into 0.5 pc, which can hide a small group of YSOs. Indeed, 10 of the YSOs are resolved by our ISPI images (with a $0\farcs3$ pixel$^{-1}$ scale) into multiple sources or even small clusters within the IRAC PSF. Another 10 YSOs appear more extended than the ISPI PSF; two of these have NACO images available and both are resolved into multiple sources. These results suggest that at least 44% and up to 74% of the IRAC-identified YSOs are multiple sources. Similarly high fractions, 50–65%, have been reported for YSOs in N44 (Paper I) and for 82 LMC YSOs which have archival *HST* H$\alpha$ images available (Vaidya et al. 2009). While the ISPI and NACO $JK_s$ images allow us to identify the dominant YSO in a multiple system for accurate photometric measurements, the IRAC measurements correspond to the integrated light of all sources within the PSF. This mismatch is not problematic if one YSO dominates the emission in IR bands; however, if two or more YSOs are present within the IRAC PSF, the SED modeling can produce very uncertain results. Below we use two examples to illustrate the extent of errors caused by multiplicity.

The YSO 053941.89−694612.0 in N 159 appears extended in the ISPI $JK_s$ images and is resolved into four sources within $0\farcs6$ in the NACO $J$ images. Among these four, the two brightest sources (#123 and #121 in N 159-A7, Testor et al. 2006), have $K_s = 13.31$ and 13.52 and $J - K_s = 4.80$ and 4.22, respectively; the extremely red colors originate from infrared excess unless the foreground extinction was exceedingly high, so these are most likely YSOs. Therefore, 053941.89−694612.0 can be used to assess uncertainties in SED fitting for cases where two YSOs of comparable properties exist within the IRAC PSF. We construct SEDs for these two bright sources, 053941.89−694612.0a and b, using $JK_s$ from Testor et al. (2006) and IRAC/MIPS fluxes proportioned according to their $K_s$ mag; the latter assumption is reasonable since both YSOs have very red $J-K_s$ colors indicating early evolutionary stages. Model fits to these two SEDs are shown in Figure 7, along with fits to the SED of integrated fluxes of the multiple system. All three SEDs have similarly good fits.

The results of the SED fits are listed in Table 7. The stellar mass inferred from the SED of integrated fluxes is 32 $M_\odot$, and those for the individual a and b components are 27 and 25 $M_\odot$, respectively. Component a makes up $\lesssim$ half of the total light in near-IR and has an inferred mass $\sim 84\%$ of that from the SED of integrated fluxes. Thus, for a source containing multiple YSOs at similar evolutionary stages such as 053941.89−694612.0, the inferred mass for individual (most massive) YSO could be overestimated by $\sim 20\%$, and the

total YSO masses may be underestimated by ∼40%.

The second example of multiplicity in a YSO source is 054004.40−694437.6 in N 159B, or the Papillon Nebula (Henize 1956; Heydari-Malayeri et al. 1999). *HST* images revealed a complex H II region around 054004.40−694437.6. Heydari-Malayeri et al. (1999) used the integrated H$\beta$ flux of the H II region (assuming ionization-bounded) and determined that the spectral type of the ionizing source(s) of N 159B is at least O8 V or earlier, while Indebetouw et al. (2004) reported an O6V ionizing star based on the integrated radio centimeter continuum flux of N 159B. The clumpy morphology seen in the *HST* images suggests that ionizing photons may leak from this region; thus the O8V spectral type is a lower limit. As illustrated in Figure 7d, our single-YSO model fails to simultaneously reproduce the mid-IR dust emission and the optical light. The latter, adopted from the relatively low-resolution MCPS catalog, is almost certainly contaminated with nebular line emission from the ionized gas that is not included in the YSO models.

To separate the central point source of 054004.40−694437.6 from the surrounding nebulosity, we use photometric measurements made with *HST* images in the optical and VLT/NACO adaptive optics images in $K_s$. At other IR bands, we use the IRSF $JH$ measurements as upper limits, and IRAC and MIPS fluxes as they are. The resultant SED and model fits are shown in Figure 7e, and the inferred YSO mass is $\sim 21\ M_\odot$ (Table 7). The SED fitting is biased toward *HST* data points as they have smaller errors compared with those of *Spitzer* data points. It is thus not surprising that the YSO mass is consistent with the B0/O9 spectral type implied by the *HST UbyI* photometry. In fact, Heydari-Malayeri et al. (1999) and Testor et al. (2007) have already suggested that the point source detected in *HST* images, which is also the brightest source in the VLT/NACO $K_s$ image within the IRAC PSF, does not account for the full luminosity or the centimeter radio flux of the nebula.

As the optically brightest star in 054004.40−694437.6 may not be the YSO contributing to the observed mid-IR emission, we decouple the mid-IR part of the SED from the rest and make SED fits to only the mid-IR segment. This is essentially using the luminosity of dust emission as a calorimeter to infer the effective luminosity of the main energizing source(s) without specifically trying to separate those sources from the H II region. The result should be consistent with the spectral type derived from the total radio continuum emission from the H II region. Figure 7f shows that the mid-IR part of the SED can be reproduced by models reasonably well, and the inferred mass, $\sim 41\ M_\odot$ (Table 7), is indeed in agreement with the O6V spectral type derived from radio observations (Indebetouw et al. 2004). Therefore, the main ionizing sources of the Papillon Nebula are still hidden behind a large amount of dust.

In summary, when a YSO is in a multiple system, it is crucial to use high-resolution optical and near-IR images to assess whether the multiple components are at different evolu-

tionary stages. If the dominant sources are at similar YSO stages, model fits of the integrated SEDs would overestimate the mass of the most massive YSO but underestimate the total mass of the YSOs. On the other hand, if multiple sources at different evolutionary stages are present, the optical and near-IR emission may be dominated by the exposed stars and the mid-IR emission dominated by more embedded YSOs. Under these circumstances, model fits to the mid-IR portion of the SED can still provide useful information on the dominant heating sources. Lastly, we note that since only one case in each of these two types of system is investigated, our estimates on mulitiplicity effect is thus approximate and a better quantification requires a larger sample. A cautionary corollary of our result is that the uncertainties would be even larger in mass estimates for YSOs of three or more comparably bright objects, such as the 5 multiple YSOs that are already resolved in the ISPI $JK_s$ images since each single source could be further resolved into multiples in even higher resolution (e.g., the aforementioned NACO) images.

## 4.4. Evolutionary Stage of YSOs

### *4.4.1. Comparisons among Empirical, Theoretical, and Spectral Classifications*

We use our analysis of 22 "single" YSOs to compare our empirical classification, Type, with the theoretical classification, Stage (Robitaille et al. 2006). As listed in Table 6, Types and Stages are only loosely correlated. This lack of overwhelming correspondence is also seen in Paper I and may be attributed to two reasons primarily related to the relatively large distance of the LMC. In an unresolved cluster treated as a single source, details of the circumstellar dust geometry may not correspond extremely well to our model prescription, making the translation of fitted dust mass into an accretion rate (quantitative Stage) less certain. On the other hand, a Type determined from environmental morphology on parsec scale may also not accurately reflect the evolutionary state of a single YSO. The methods are both useful, neither definitive. Second, limited angular resolution may cause inclusion of extraneous dust emission from unresolved H II regions. This is particularly relevant to YSOs at a late evolutionary stage, such as the three Type III YSOs that show small H II regions in the MOSAIC H$\alpha$ images; the mid-IR emission from unresolved H II regions would have been erroneously modeled as circumstellar disks or envelopes. Nevertheless, we expect the extreme Stage I YSOs to correspond to our Type I YSOs, since they are deeply embedded in massive envelopes. Indeed, Table 6 shows that Type I YSOs are well fitted by Stage I models. We also expect Type III YSOs without H II region confusions to correspond to Stage III YSOs, and indeed this is the case for 054000.69−694713.4.

We also use the 11 YSOs with IRS observations to compare our empirical classification

with the classification based on spectral features (Seale et al. 2009). Table 8 lists their spectral classification and the presence of silicate absorption. Among the 11 YSOs, 10 have spectral type PE, whose spectra show PAH and fine-structure line emission, and 1 has spectral type P, whose spectrum shows PAH emission but not fine-structure line emission. Our empirical classification for the 10 YSOs with PE-type spectra cover Types I, I/II, II, and III, indicating that the ionized gas can be present early on. Compared with PE-Type YSOs, the P-Type YSOs may have an earlier evolutionary stage because of a higher accretion rate that quenches the formation of an H II region or have a stellar temperature too low to provide ionizing flux (Seale et al. 2009). The P-type YSO in N 159, 053929.21−694719.0, is classified as Type I, and additional evidence is presented in §4.4.2 to suggest that this P-type YSO is in an earlier evolutionary stage than the PE-Type YSOs. The strongest spectral feature that correlates with our empirical classification is the silicate absorption. The presence of silicate absorption is an indication of early evolutionary stage (Seale et al. 2009). The five YSOs in N 159 that show silicate absorption are all of Types I and I/II. They are also all of Stage I and have high $\dot{M}_{\rm env}$, $7.0 \times 10^{-4} - 4.6 \times 10^{-3} M_{\odot}$/yr (Table 6), inferred from SED modeling, bolstering their evolutionary stage being early. Thus, our classification using multiwavelength SEDs and images suggests an evolutionary sequence consistent with that implied by classification based on spectra features.

### *4.4.2. Evolutionary Stages of YSOs Associated with Masers and Ultracompact H II Regions*

Massive stars inject energy into the surroundings even during their formation. They undergo energetic mass ejection in the form of molecular outflows and produce maser phenomenon. They can also ionize the circumstellar gas to form small, dense H II regions such as ultra-compact H II regions (UCHIIs) with diameters $\leq 10^{17}$ cm and densities $\geq 10^{4}$ cm$^{-3}$ (Franco et al. 2000). In N 159, a $H_2O$ maser source and three UCHIIs have been identified (Lazendic et al. 2002; Indebetouw et al. 2004), and each of these four objects is spatially coincident with a massive YSO (Figure 8a). The link between these objects and YSOs allows us to compare the YSOs' evolutionary stages inferred from SED models to the circumstellar conditions required to form masers or UCHIIs, providing an independent check for the feasibility of SED models.

The $H_2O$ maser in N 159 was first reported by Hunt & Whiteoak (1994) and confirmed with subarcsecond resolution and accurate position by Lazendic et al. (2002). It coincides with our Type I YSO 053929.21−694719.0 within 1″. As listed in Table 9, this YSO has a high mass of 26.1±1.5 $M_{\odot}$ and a high $\dot{M}_{\rm env}$ of (5.1±1.5)×$10^{-4} M_{\odot}$ yr$^{-1}$ derived from model

fits to its SED. The high $\dot{M}_{\rm env}$ indicates it as a Stage I YSO. Its IRS spectrum is classified as Type P (Table 8), as it does not show any fine structure lines from ionized gas (Seale et al. 2009). The high mass of the stellar core implies that it does emit ionizing radiation; however, the high envelope accretion rate suggests that the circumstellar H II region is most likely too small to become detectable with our large beam. The analysis of the YSO's SED leads to the conclusion that YSO 053929.21−694719.0 is in an early evolutionary stage. Indeed, it is commonly accepted that the water maser phase precedes the UCHII phase (Ellingsen et al. 2007). Therefore, the production of the water maser and the YSO's SED models all point to a consistent picture that 053929.21−694719.0 is at a very young evolutionary stage.

Three UCHIIs have been identified in N 159: B0540−6946(1), B0540−6946(4), and B0540−6946(5) (Indebetouw et al. 2004). All three UCHIIs are coincident with *Spitzer* sources within 1″, and these sources have been identified as Type I, II/III, and III YSOs (Table 9). As these sources are among the five most luminous YSOs in N 159 at 8.0 $\mu$m, they are also bright in the 24 and even 70 $\mu$m images from which reliable measurements are needed to constrain model fits to their SEDs. The stellar luminosities determined from the best-fit SED models can be translated into spectral types, assuming the relationship for main sequence stars. These spectral types can be compared with those implied by the ionizing fluxes determined from radio continuum observations (Indebetouw et al. 2004). As seen in Table 9, agreement exists between the spectral types independently determined with these two methods.

The development of a UCHII depends on not only the ionizing flux provided by the central star, but also the opacity of the circumstellar medium. For infalling rates higher than some critical value, $\dot{M}_{\rm crit}$, the circumstellar medium will have such high opacities that the ionized region will be too small and too optically thick to be detectable (Churchwell 2002). For the respective spectral types of the central stars, the $\dot{M}_{\rm crit}$ of the three UCHIIs in N 159 are computed to be $\sim 3 - 7 \times 10^{-5} M_{\odot}$ yr$^{-1}$ (Table 9). Compared to the $\dot{M}_{\rm env}$ determined from the best-fit models (Table 6) or weighted average $\dot{M}_{\rm env}$ determined from all accepted models (Table 9) for these three YSOs, it is seen that all three YSOs have $\dot{M}_{\rm env} \gg \dot{M}_{\rm crit}$. We have further examined whether any acceptable models of the three YSOs yield smaller envelope accretion rates. We find that all the other acceptable models have $\dot{M}_{\rm env} \gg \dot{M}_{\rm crit}$. This is similar to that found for 3 of the 4 UCHIIs associated with YSOs in N 44 (Paper I).

There could be two causes for $\dot{M}_{\rm env} \gg \dot{M}_{\rm crit}$. One is that most of the infalling envelope material is used in forming an accretion disk as modeled by Yorke & Sonnhalter (2002), and the ionizing radiation escapes in the polar directions. The other is that at the LMC distance, it is difficult to distinguish bound, circumstellar dust from more distant but still

heated interstellar dust. The warm envelope of an UCHII contributes to the mid-IR emission modeled in the SED, and raises the derived accretion rate. Thus, the high envelope accretion rates of YSOs associated with these UCHIIs and the $H_2O$ maser mostly suggest that they still have abundant dust/gas in the surroundings and have not significantly cleared their environments. In terms of evolutionary sequence, we find that the maser is associated with Type I while UCHIIs are associated with Types I, I/II, and III; this is consistent with the general picture that the maser phase happens earlier than UCHII (Ellingsen et al. 2007). Although the SED of the maser source is probably also contaminated by hot dust in the environment that may not actually accrete onto the protostar.

#### *4.4.3. Evolutionary Stages of YSOs as Herbig Ae/Be stars*

HAeBe stars are intermediate-mass young stars that have evolved from the most embedded phase and are now revealing their stellar components (e.g., Hillenbrand et al. 1992). Since our YSO sample overlaps this mass range, we examine whether some of them might be previously classified as HAeBe stars. Candidate HAeBe stars in N 159 have been selected by Nakajima et al. (2005) using near-IR $JHK_s$ photometry. Figure 8a shows their locations marked on an 8 $\mu$m image of N 159, along with our YSOs marked in different colors to indicate their evolutionary stages. Figure 8b and c show color-color and color-magnitude diagrams using $JHK_s$ photometry of sources in N 159 that are detected in all three bands (kindly provided by Yasushi Nakajima; Nakajima et al. 2005). As listed in Table 8, nine of these candidate HAeBe stars are identified as YSOs and they have the following types of SEDs: one Type I, one Type I/II, five Type II, and two Type III. The majority (78%) of these HAeBe candidates are Type II and III YSOs, consistent with the expectation that such objects are less embedded. There are also two candidate HAeBe stars that we classify as non-YSO sources: 053921.21−694409.4 is a star superposed on dust clumps, and 053938.80−694436.0 is the O7 III stellar counterpart of the high-mass X-ray binary LMC X-1 (Cowley et al. 1995). The latter clearly is not a young star, and this explains why its colors are bluer than the other HAeBe stars (see Figure 8b and c).

### 4.5. Masses of YSOs

The mass estimates from the best and acceptable fits of 27 YSOs in N 159 are listed in Table 6. Among them, 22 YSOs have single or dominant sources within the IRAC PSF and their SEDs can be properly approximated by single-YSO models to obtain reliable mass estimates. The other five have SEDs from multiple YSOs or even non-YSO sources such as

stars or nebulosities; their mass estimates have larger uncertainties and should be viewed as rough estimates. Nevertheless, the results of SED fits show that twenty of the YSOs in N 159 have $\chi^2$-weighted average mass greater than 8 $M_\odot$ and thus are most likely bona fide massive YSOs. The remaining seven have $\chi^2$-weighted average $< 8$ $M_\odot$ and are likely intermediate-mass YSOs.

It has been suggested that the criterion $[8.0] \leq 8.0$ may be used to select massive YSOs in the LMC (Gruendl & Chu 2009). We find that indeed the $\chi^2$-weighted average mass of the brightest YSOs, with $[8.0] \leq 8.0$, are all $\geq 8$ $M_\odot$. This criterion may be too conservative, as all (15 out of 15) YSOs with $[8.0] \leq 9.0$ still have masses $\geq 8$ $M_\odot$ The results are consistent with what we found for YSOs in N 44 (Paper I).

At the high-mass end, nine YSOs have $\chi^2$-weighted average mass $> 17$ $M_\odot$; these are most likely O-type YSOs. Two YSOs have $\chi^2$-weighted average mass close to 17 $M_\odot$ and larger standard deviation that extending beyond 17 $M_\odot$; these may or may not be O-type stars. Therefore, there exist at least 9 O-type YSOs in N 159. These most massive YSOs will be discussed further in §5.1.

## 5. Massive Star Formation in N 159

It is difficult to study the relationship between interstellar conditions and the formation of massive stars because massive stars' UV radiation fluxes and fast stellar winds quickly ionize and disperse the ambient ISM. Young massive YSOs that have not significantly altered the physical conditions of their large-scale environments can be used to probe massive star formation. The large number of massive YSOs found in N 159 provides an excellent opportunity to investigate issues such as the relationship between star formation properties and interstellar conditions, progression of star formation, and evidence of triggered star formation.

### 5.1. Interstellar Environments and Star Formation Properties

We examine the star formation properties of the molecular clouds in N 159 as these clouds contain the bulk material to form stars. The SEST and MAGMA CO surveys of the LMC (Johansson et al. 1998; Ott et al. 2008) show three large concentrations of molecular material in N 159, i.e., the eastern, western, and southern peaks (Figure 9). These three concentrations exhibit different numbers of massive stars formed in the last 10 Myr, as evidenced by their different amounts of ionized gas. The eastern molecular peak is associated

with bright H$\alpha$ emission from the prominent central H II regions. Star formation has been occurring in this $\sim 35$ pc $\times$ 50 pc region for an extended period of time, as it contains both evolved and young massive stars. For example, star #54 of Fariña et al. (2009) is a B1-2 IV-II star that is $\sim 10$ Myr old, while their star #62 is an O4-6 Vn star that is $\lesssim 3$ Myr old (Schaerer et al. 1993; Schaerer & de Koter 1997). The western molecular peak has only several small, disjoint H II regions, but one of them, N 159A, has the highest H$\alpha$ surface brightness in the entire N 159. The massive stars in N 159A and its surroundings have been imaged in $UBV$ and their colors and magnitudes indicate that their spectral types range from B2 V to O5–6 V (Deharveng & Caplan 1992). Given the absence of SNRs, these stars are most likely $\lesssim 5$ Myr or that star formation started only in the last few Myr. The southern molecular peak only has a couple of small H II regions, indicating that only modest massive star formation has taken place.

Figure 9 shows that 96% (= 26/27) of YSOs in N 159 are found within CO contours $\geq$ 1 K km s$^{-1}$. This corresponds to an $H_2$ column density of $\geq 4 \times 10^{20}$ cm$^{-2}$, for a CO-to-$H_2$ conversion factor $X_{\rm CO} = 3.9 \pm 2.5 \times 10^{20}$ cm$^{-2}$ (K km s$^{-1}$)$^{-1}$ in the molecular ridge which includes N 159 (Pineda et al. 2009). About 70% of the YSOs are congregated toward the three molecular peaks, similar to the 75% found in N 44 (Paper I). The YSOs of the three molecular peaks show different characteristics in their spatial distributions and interstellar environments. The western molecular peak has the highest concentrations of YSOs, as 12 YSOs are found within $\sim 1\farcm5$ (= 22 pc)-radius of the CO contour peak and 6 of them cluster in a small region of $40'' \times 80''$ (=10 pc $\times$ 20 pc) over the bright H II region N 159A and its north tip N 159AN. The eastern molecular peak has more widely distributed YSOs, and most of them are associated with H II regions. The southern molecular peak has 4 YSOs that are loosely distributed, and they are not associated with any ionized gas.

The YSOs of the three molecular peaks in N 159 also show differences in their mass distributions. In Figure 9, we have marked the YSOs with circles in three sizes that represent O-type stars with inferred $\bar{M}_\star \geq 17 M_\odot$, (early) B-type stars with $17 > \bar{M}_\star \geq 8 M_\odot$, and intermediate-mass stars with $\bar{M}_\star < 8 M_\odot$. We found $\sim 80$% of the O- and B-type YSOs in N 159 are in or adjacent to H II regions, similar to those seen in N 44 (Paper I). The YSOs with intermediate masses or without mass estimates do not show such preferred association with H II regions, but this may be caused by an observational bias against the detection of these fainter intermediate-mass YSOs over the bright background dust emission in H II regions. The western and eastern molecular peaks, associated with bright H II regions, have a respectable number of O- and B-type YSOs, while the southern molecular peak has one YSO with mass $\sim 8 M_\odot$ and no O-type YSOs at all.

Similar to the trend seen in N 44 (Paper I), the characteristics of the current star for-

mation in the three molecular peaks of N 159 appear to be dependent on the massive star formation that occurred in the recent past. We have further examined whether the pattern of star formation is related to the physical properties of molecular clouds. The eastern, western, and southern molecular concentrations contain GMCs N 159-E, N 159-W+N 159-2, and N 159-S+N 159-3, respectively (Johansson et al. 1998). Their physical properties adopted from Johansson et al. (1998) are listed in Table 10, including each GMC's local standard of rest velocity ($V_{\rm lsr}$), CO line-widths ($\Delta V$), virial mass ($M_{\rm vir}$), luminosity mass ($M_{\rm lum}$), and ratio of virial to luminosity mass. Note that $M_{\rm lum}$ is converted from the CO luminosity $L_{\rm CO}$ using $M_{\rm lum} = 8.8 \pm 5.6 L_{\rm CO} M_{\odot}$, revised from Equation (6) in Bolatto et al. (2008) for an $X_{\rm CO}$ value suitable for N 159 (Pineda et al. 2009). In addition, when there are two GMCs in a molecular concentration, we use averages of $V_{\rm lsr}$ and $\Delta V$ and sums of $M_{\rm vir}$ and $M_{\rm lum}$, respectively, to represent the properties of a concentration. For comparisons, in Table 10 we have also listed these quantities for GMCs in N 44 (Mizuno et al. 2001), where the $M_{\rm lum}$ is converted from the CO luminosity $L_{\rm CO}$ using $M_{\rm lum} = 15.8 \pm 4.5 L_{\rm CO} M_{\odot}$ for $X_{\rm CO} = 7 \pm 2 \times 10^{20}$ cm$^{-2}$ (K km s$^{-1}$)$^{-1}$ (Fukui et al. 2008).

The GMC N 159-W has the smallest $\Delta V$ and $M_{\rm vir}/M_{\rm lum}$ ratio, which can be an indicator of lower gravitational support, and contains the largest number and most concentrated distribution of massive YSOs. Similarly, the GMC N 44-C has YSO properties like N 159-W and also has a smaller $M_{\rm vir}/M_{\rm lum}$ ratio among the GMCs in N 44. The larger sample of 36 LMC GMCs in Indebetouw et al. (2008) showed a similar trend of more star formation activity at lower $M_{\rm vir}/M_{\rm lum}$. This may reflect preferred physical conditions for GMCs to collapse and form a concentrated cluster, qualitatively consistent with the picture that a smaller turbulent kinetic energy results in larger volumes exceeding the Jeans criterion for gravitational instability (e.g., Klessen et al. 1998). The similar values in $\Delta V$ and $M_{\rm vir}/M_{\rm lum}$ ratios found in the other two GMCs in N 159 do not seem to scale with their different star formation activity, although the uncertainties in the virial analysis are large compared to the differences between the GMCs. Detailed mapping of these three GMCs could reveal some of the physics underlying their different star formation characteristics. In particular, observations of denser gas tracers such as $HCO^+$ and HCN reveal the virial ratios and physical conditions of the *clumps* that are actively participating in star formation, whereas bright CO emission can also come from more diffuse or photo-dissociation regions of the GMC. High-resolution ($\sim 5''$) $HCO^+$ observations of N 159-E and W have shown that dense clumps are spatially correlated with YSOs at early evolutionary stage (Chen et al, 2010, in preparation), and new observations of N 159-S taken in October 2009 will reveal whether dense clumps are present in this GMC as well.

### 5.2. Massive Star Formation – Triggered or Spontaneous?

A number of observational studies have demonstrated that the current star formation may be triggered by stellar energy feedback, such as through the expansion of an H II region (e.g., Zavagno et al. 2007; Pomarès et al. 2009). N 159 experiences intense energy feedback evidenced with the filamentary structure in the H II regions (Figure 1) and the existence of SNR 0540−697 (Chu et al. 1997; Williams et al. 2000). N 159 also has abundant molecular material for continued star formation. It is conceivable that its (main-sequence) massive stars photonionize the ambient gas to form H II regions and the raised thermal pressure can compress the neighboring molecular cloud to trigger star formation. In fact, as shown in Figure 9, about 2/3 of the YSOs are associated with H$\alpha$ emission and almost all of them are in the eastern and western GMCs. In contrast, none of the four YSOs in the southern GMC are associated with H II regions. To investigate whether some of the current star formation in the eastern and western molecular concentrations may have been triggered, we compare the distributions of YSOs relative to the massive stars, and use high-resolution MOSAIC H$\alpha$ images to examine the immediate environment of YSOs.

The eastern GMC is associated with the prominent central H II regions in N 159. This region has 17 spectroscopically identified massive stars (Fariña et al. 2009). As shown in the MOSAIC H$\alpha$ image in Figure 10a, these massive stars are distributed in the bright northern and southern lobes of the central H II region, while the YSOs are mostly found along the edges of an east-west oriented low-surface-brightness band between the two lobes. As this band coincides with the peak of the GMC, the spatial distributions of YSOs appear to suggest that their formation is likely triggered by the expansion of two H II regions (lobes) into a central molecular cloud. To test this hypothesis, we used two methods to search for massive stars in the central molecular cloud that were formed earlier before the external pressure was raised but are too obscured to be detected at optical wavelengths.

We first use the 3 cm map to search for obscured O stars, since it is nearly extinction-free signpost of gas ionized by massive stars. Figure 10a reveals that the 3 cm emission of N 159 (Dickel et al. 2005; Seward et al. 2010) appears diffuse for a 22″ resolution over (mature) massive stars in the bright H II regions, but shows four peaks in the east-west central band and the western molecular concentration. Three of the four 3 cm peaks are centered at O-type YSOs associated with UCHIIs (Indebetouw et al. 2004). The remaining 3 cm peak, i.e., the faintest peak in the east-west band, is centered between two non-O-type YSOs and has no UCHIIs detected. The absence of UCHIIs indicates that these YSOs have lower masses than the detection limit of a B0 V star, or that the H II regions of optically obscured OB stars are too extended and thus resolved out by the small synthesized beam (Indebetouw et al. 2004).

We next consider the candidate OB stars identified with $JHK_s$ photometry (Nakajima et al. 2005). Figure 10b shows that some of them are distributed around, though not inside the east-west band. To assess whether there might be OB stars hidden by extinction even in the near-IR, we use the H$\alpha$ and 3 cm maps to estimate the extinction. Assuming that the 3 cm emission of N 159 is completely thermal[3], the extinction in the H$\alpha$ emission, $A_{\rm H\alpha}$, of a 10,000 K H II region can be estimated using

$$A_{\rm H\alpha} = -2.5\log\ (\frac{F_{\rm H\alpha}}{S_{\rm 3cm}}/\frac{j_{\rm H\alpha}}{j_{\rm 3cm}}), \quad (1)$$

where $j_{\rm H\alpha}/j_{\rm 3cm} = 8.86\times10^{-10}$ ergs cm$^{-2}$ s$^{-1}$ Jy$^{-1}$ and then converted to the visual extinction using $A_V = 1.24A_{\rm H\alpha}$ (Caplan & Deharveng 1986). Figure 10b shows the visual extinction map and its peak value is $\lesssim$ 5.0 in the east-west band. For a standard extinction curve of $A_J/A_V = 0.28$ and $A_K/A_V = 0.11$, an O8 V star would have $J = 16.1$ and $K = 15.1$ (Schmidt-Kaler 1982; Koornneef 1983), brighter than the catalog's 10-$\sigma$ limiting magnitudes of $J = 18.8$ and $K = 16.6$ (Nakajima et al. 2005), and would have been detected if the local variation in the extinction is within a factor of 3, i.e., $A_V \sim 15$. As for massive YSOs which usually have [8.0] $\leq$ 9.0, a foreground extinction of $A_V = 5.0$ corresponds to $A_{8.0} = 0.24$ (Indebetouw et al. 2005) and imposes little effect on their detection. The above considerations suggest that the peak of the eastern GMC was not active in producing O-type stars a few Myr in the past and only began to form them currently in locations on the edges contacting H II regions. Thus, the formation of the YSOs in the GMC N 159-E is likely triggered.

It is interesting to note that YSOs 054003.49−694355.0 and 054004.40−694437.6 in NGC 159-E are projected within and at the edge of SNR 0540−697 (Figure 10a). For this SNR to be responsible for the formation of these two YSOs, its age has to be longer than the ages of YSOs. The age of this SNR, estimated from its size and expansion velocity, is $\sim 1 - 2 \times 10^4$ years (Williams et al. 2000). The absolute ages of the YSOs are difficult to estimate. However, the brighter and more massive of the two YSOs, 054004.40−694437.6, has formed a small H II region visible in the optical wavelength, i.e., the Papillon Nebula (Heydari-Malayeri et al. 1999), and hence its age is likely to be more than several $10^5$ years (Churchwell 2002). The fainter and less massive of the two YSOs has evolved beyond the earliest evolutionary stage and thus unlikely to be younger than a few $10^5$ years. The age consideration suggests that the SNR is unlikely to be responsible for the formation of these two YSOs.

[3]This assumption is likely to result in an overestimate of the extinction as there is contamination of non-thermal emission from the nearby SNR 0540−697 (Seward et al. 2010).

The western GMC in N 159 abuts the central H II regions. For the expanding H II regions to trigger star formation in this molecular concentration, the crossing time scale should be shorter than the ages of massive stars and YSOs. Figure 10a shows that the boundary of the H II regions is $\gtrsim 40''$, or a projected distance of 10 pc from the massive stars and YSOs. For this distance and a velocity dispersion $\sigma$ of 2.6 km s$^{-1}$ of the GMC N 159-W (from $\sigma = 0.43\Delta V$ and $\Delta V = 6$ km s$^{-1}$, Johansson et al. 1998), the traverse time is $\sim 4$ Myr. This time scale is not shorter than the age of OB stars in the bright nebular component N 159A, $\sim 3 - 4$ Myr, indicated by the presence of a spectroscopically identified O8 star and a few photometrically identified mid- to late-O stars (Deharveng & Caplan 1992; Schaerer & de Koter 1997; Fariña et al. 2009). Thus it is not likely that the expansion of the central H II regions is responsible for the formation of these massive stars. Furthermore, YSOs in the western GMC are concentrated in the molecular core, in contrast to the YSOs in the eastern GMC that are spread out and distributed along the interface between the molecular cloud and H II region.

It has been suggested that the star formation in N 159 started near the center of the diffuse radio emission where OB stars identified with $JHK$ photometry are located, and proceeded outwards to trigger next-generation star formation in the eastern and western GMCs (e.g., Jones et al. 2005; Nakajima et al. 2005). Our detailed analysis finds a more complicated pattern of star formation. The expansion of the central H II region has triggered the star formation in the eastern GMC, but not the western GMC. It is possible that the star formation in the western GMC was triggered by some force that is no longer identifiable, such as an old SNR whose shock velocity had slowed down to 20–45 km s$^{-1}$ (Vanhala & Cameron 1998). It is also known that in an active star forming region, the environment is usually too complex to pinpoint the triggering mechanism for star formation (Desai et al. 2010). Nevertheless, based on the distribution of YSOs concentrated near the core of the western GMC as well as its lowest velocity dispersion (kinetically cold) among GMCs in N 159, we suggest that its star formation may have started spontaneously. This suggestion is further supported by the most massive stars formed in the western GMC, as shown below.

A trend is observed in YSOs in H II regions in the Milky Way and the LMC that in triggered star formation, the second generation is less massive than the first (e.g., Pomarès et al. 2009; Fleener et al. 2010). In N 159, the most massive YSO formed in the eastern GMC, 054004.40−694437.6, is O6 V (Indebetouw et al. 2004), not as massive as the earliest type O4-6 Vn found in the central H II region (#54 in Fariña et al. 2009). The most massive YSO formed in the western GMC, 053937.53−694609.8, is O5.5V (Indebetouw et al. 2004), more massive than the only spectroscopically classified O8 star[4] in the bright H II region N 159A

[4]Deharveng & Caplan (1992) suggested another star as mid- to late-O type based on its $UBV$ colors and

(Fariña et al. 2009). The spectral types derived from radio continuum by Indebetouw et al. (2004) may be underestimates if significant ionizing flux is leaking from the UCHII, and there is a systematic uncertainty in converting from ionizing flux to spectral type due to differences in massive stellar atmosphere models. However, the comparison of most massive YSOs and main-sequence stars in these two GMCs suggests that the eastern GMC is more consistent with the aforementioned trend than the western GMC. In cases of spontaneous star formation, the masses of YSOs do not depend on the masses of stars that were formed earlier in the molecular cloud. It is thus the cloud properties that determine the types of stars formed, though once massive stars are formed, their energy feedback can trigger further massive star formation as demonstrated in the eastern GMC. These two factors can naturally result in massive YSOs preferentially found in GMCs associated with H II regions as the GMCs likely already have conditions to form massive stars and can form even more with the aide of stellar energy feedback.

### 5.3. Star Formation Efficiency and Rate

The correlation or lack thereof between GMC properties in galaxies and their star formation activity is of critical importance to understand galaxy evolution and star formation in general. In particular, we need to understand the physics underlying the empirically observed correlation between star formation rate and gas surface density, the "Schmidt-Kennicutt" (S-K) relation (e.g., Kennicutt 1989; Calzetti et al. 2007; Kennicutt et al. 2009). This correlation is tight when properties are averaged over a kpc or more, but it is difficult to justify why it should hold on sub-kpc scales. Only recently have datasets been rich enough to explore the smaller scales. The THINGS project (Walter et al. 2008) found that whether molecular or total (= molecular + atomic) gas surface density is a better predictor of star formation depends on which is the dominant phase in that part of the galaxy (Leroy et al. 2008), and in molecular regions, star formation scales linearly with $H_2$ surface density (Bigiel et al. 2008).

Large-scale star formation in a galaxy depends on the formation rate of GMCs and how GMCs collapse to form stars. Theoretical models assuming that GMCs have a constant star formation efficiency within a free-fall timescale find that GMC formation is the dominant driver in the star formation rate (SFR) in galaxies, and that the S-K relation can be reproduced (Krumholz et al. 2009). It is of fundamental importance to determine how and when GMCs collapse to form stars. Only a small number of detailed extragalactic studies have

magnitudes, however such conversion is known to have large uncertainties (e.g., Massey 1985).

been made. In N 44 (Paper I), N 159 (this study), and the LMC's quiescent molecular ridge (Indebetouw et al. 2008), we find that although most massive young stars are found near peaks in $^{12}$CO emission, there is not always a clear correlation between $^{12}$CO properties and YSO properties. In N 44 and N 159, massive YSOs are mostly found in GMCs associated with ionized gas. In N 44, the most massive GMC N 44-S has $\sim$ 5-times the cloud mass but only half the YSO content of N 44-C; in N 159, the most massive GMC N 159-S formed only a few YSOs and none of them are massive (Table 10). The current star formation activity appears to correlate more with the energy feedback from antecedent massive stars than the mass of a GMC. Indebetouw et al. (2008) found that in the molecular ridge, the SFR measured from either integrated mid-IR light or detailed analysis of the YSOs is correlated with the $M_{\rm vir}/M_{\rm lum}$ ratio, an indicator of gravitational support. However, the total SFR measured from the integrated light is far below that expected from the S-K relation for the given GMC surface density. The molecular ridge is known for its anomalously low star formation activity, but the GMCs in N 44 and N 159 host a range of star formation activities and may be used to investigate whether the S-K relation applies on scales of individual GMCs.

The known massive YSO content allows us to assess the instantaneous star formation efficiency, $\rm SFE_{YSO}$, of a GMC. We use the number counts of YSOs within different mass bins and the assumption of Salpeter's initial mass function (IMF) to estimate the total mass of the current star formation, $M_{\rm YSO}^{\rm total}$. The lowest mass bin used for counting depends on the photometric completeness in a region. For regions with bright diffuse background, such as N 159-W and N 44-C, only higher-mass bins are used to avoid problems from photometric incompleteness at $< 9.0$ mag, though at the expense of small number statistics. The brightness limit [8.0]= 9.0 corresponds to $\sim 8 M_\odot$ (recall masses of YSOs inferred from SED fits in §4.5). The total mass, $M_{\rm YSO}^{\rm total}$, is calculated by integrating the initial mass function from $M_{\rm l}$ = 1 $M_\odot$ to $M_{\rm u}$, the highest mass of YSO observed. We adopt the commonly used lower mass limit of 1 $M_\odot$ to facilitate comparisons with other work, although the formation time scale of a 1 $M_\odot$ star is much longer than that of the observed massive YSOs. The $M_{\rm YSO}^{\rm total}$ is then divided by the virial mass of the GMC ($M_{\rm vir}$) to obtain $\rm SFE_{YSO}$, and all these three quantities are listed in Table 10. Uncertainties in $M_{\rm YSO}^{\rm total}$ are also listed; they are directly related to the uncertainty in mass inferred for individual massive YSOs used in number counts and are thus estimated from the largest and small mass ranges covered by these massive YSOs.

To determine the SFR from the total mass of current star formation requires a timescale. Although we can constrain the age of each massive YSO from its evolutionary stage, statistics of solar-mass YSOs in Class I, II, III, and models of high-mass protostellar accretion, such ages are quite uncertain aside from being $\lesssim$ 1 Myr. On the other hand, since we consider all YSOs with high and intermediate masses within each GMC that are currently forming in a burst, this seems more relevant to the formation timescale of a cluster or association.

Proceeding with this assumption and assigning a cluster formation time ($t_{\rm cluster}$) of $\sim 1$ Myr (e.g., Bonnell et al. 2003), we derive the current star formation rate, $\rm SFR_{YSO}$. We have also estimated SFE per free-fall time ($t_{\rm ff}$),

$$\epsilon_{\rm ff} = \frac{t_{\rm ff}}{t_{\rm cluster}} \frac{M_{\rm YSO}^{\rm total}}{M_{\rm vir}} \tag{2}$$

(e.g., Huff & Stahler 2007) which has gained popularity recently as a normalized measure of star formation activity. Note that the angular resolution for CO data of N 44 and N 159 are different: N 44 was observed at 145″ angular resolution while N 159 at 45″ resolution. Thus, in N 44, multiple GMCs may not be resolved, resulting in much larger GMC size and longer $t_{\rm ff}$. Table 10 shows that the $\rm SFE_{YSO}$ for GMCs in N 44 and N 159 are low, $\sim 0.0002 - 0.009$. As a comparison, the molecular cloud associated with the Pipe Nebula, a very low-level Galactic star formation region, has $\rm SFE_{YSO} \sim 0.0006$ for YSOs $\geq 0.3 M_\odot$ (Forbrich et al. 2009); the $\rm SFE_{YSO}$ found in N 44 and N 159, after multiplied by a factor of 1.7-2 to account for a lower mass limit extending to $0.3 M_\odot$ under the Salpeter's IMF assumption, are $\sim 1-25$ times that in the Pipe Nebula. The $\epsilon_{\rm ff}$ is also low, mostly $\sim 10^{-4}$ to $10^{-3}$.

For comparison, we have also estimated the SFR associated with each GMC using integrated H$\alpha$ and 24 $\mu$m fluxes with the prescription of Calzetti et al. (2007),

$$\rm SFR_{H\alpha+24}(M_\odot\ yr^{-1}) = 5.3 \times 10^{-42}[L(H\alpha)_{obs} + (0.031 \pm 0.006) L(24\ \mu m)], \tag{3}$$

where $L$(H$\alpha$) and $L$(24 $\mu$m) are H$\alpha$ and 24 $\mu$m luminosities in ergs s$^{-1}$, respectively. To measure the H$\alpha$ and 24 $\mu$m luminosities, we use an aperture size to include the bulk of a GMC; the largest uncertainties come from flux calibration, i.e., 5-10% in H$\alpha$ and 10% in 24 $\mu$m (Sean Points, private communication; MIPS Data Handbook). The aperture size, H$\alpha$ and 24 $\mu$m luminosities, $\rm SFR_{H\alpha+24}$ in $M_\odot$ yr$^{-1}$, and normalized $\rm SFR_{H\alpha+24}$ in $M_\odot$ yr$^{-1}$ kpc$^{-2}$ are all given in Table 10. Among the 6 GMCs, three have $\rm SFR_{YSO}$ higher than $\rm SFR_{H\alpha+24}$. Two of these three GMCs, N 44-N and N 159-S, have low star formation activities in the optical and near-IR wavelengths, similar to that seen in the molecular ridge (N 159-S is at the north tip of the molecular ridge). As suggested in the study of molecular ridge (Indebetouw et al. 2008), such difference likely results from the lower luminosity to mass ratios in the regions studied. In N 44-N and N 159-S, star formation occurred mostly in lower-mass or less rich clusters. As these clusters do not fully sample the high-mass end of the stellar initial mass function, they have a lower luminosity to mass ratio than the rich clusters, which are analyzed in Calzetti et al. (2007). In GMCs like N 44-N and N 159-S, $\rm SFR_{H\alpha+24}$ would severely underestimate the star formation rate by almost an order of magnitude. The third GMC with $\rm SFR_{H\alpha+24} < SFR_{YSO}$, N 159-W, has massive main-sequence stars, and it is still actively forming new massive stars (§5.2), similar to the three GMCs with $\rm SFR_{H\alpha+24} >$

$SFR_{YSO}$. The ratios of current-to-past massive star formation rates, $SFR_{YSO}/SFR_{H\alpha+24}$, of these four GMCs range from 0.4 to 2.1. These ratios suggest that the current star formation rate may be lower or even higher than the average star formation rate in the last few Myr, not constant over time. In active star forming GMCs, $SFR_{H\alpha+24}$ would miss the current star formation, which amounts to 30–70% of the total star formation rate (calculated from the above four GMCs).

Finally, we use the star formation properties of the GMCs to evaluate the S-K relation. The normalized SFR expected from the S-K relation for a region is:

$$\mathrm{SFR}(M_\odot\ \mathrm{yr}^{-1}\ \mathrm{kpc}^{-2}) = 2.5 \times 10^{-4} (\frac{\Sigma}{M_\odot\ \mathrm{pc}^{-2}})^{1.4} \quad (4)$$

where $\Sigma$ is the sum of molecular and atomic gas surface densities (Kennicutt 1998). The average molecular surface densities are measured from CO maps, adopting $X_{\mathrm{CO}} = 7 \times 10^{20}$ and $3.9 \times 10^{20}$ cm$^{-2}$ (K km s$^{-1}$)$^{-1}$ for N 44 and N 159 from Fukui et al. (2008) and Pineda et al. (2009), respectively. The atomic surface densities are measured from HI maps (Kim et al. 2003). Then the expected SFRs from the total gas surface densities, $SFR_\Sigma$, are given in Table 10. As shown in Figure 11, among the six GMCs, four of them have $SFR_\Sigma$ and $SFR_{H\alpha+24}$ in agreement within a factor of 3. The remaining two GMCs, N 44-N and N 159-S, have $SFR_\Sigma \sim 11$ and 56 times $SFR_{H\alpha+24}$, respectively. When compared with $SFR_{YSO}$, which is a better estimate of SFRs in these two low-luminosity regions, N 44-N is within a factor of 2 of $SFR_\Sigma$, while N 159-S is still only 1/5 $SFR_\Sigma$. The GMC N 159-S appears very different from the other five GMCs as its star formation rate, estimated with a comprehensive YSO inventory, is still much lower than that expected from the S-K relation. It is known that the S-K relation does not apply to small regions; thus is is not surprising that these GMCs with region sizes ranging from 45 to 135 pc do not follow the S-K relation in star formation. It is interesting that the SFR averaged over all GMCs within the entire N44 complex or the entire N159 complex is very close to that expected from the S-K relation.

## 6. Summary

We have studied the H II complex N 159 in the LMC with *Spitzer* IRAC and MIPS data at 3.6, 4.5, 5.8, 8.0, 24, 70, and 160 $\mu$m and CTIO Blanco 4 m ISPI in the $JK_s$ and MOSAIC in the H$\alpha$ bands. Following procedures outlined in Paper I, we first identified YSOs using the criteria $[4.5]-[8.0] \geq 2.0$ to exclude normal and evolved stars and $[8.0] < 14.0-([4.5]-[8.0])$ to exclude background galaxies. A total of 52 YSO candidates were identified. We then inspected the SED and close-up images of each YSO candidate in H$\alpha$, $VRIJK_s$, IRAC, and MIPS bands simultaneously to further identify evolved stars, galaxies, and dust clumps,

resulting a sample of 27 YSO candidates that are most likely bona fide YSOs of high and intermediate masses. We classified these YSOs into Type I, II, and III according to their SED shapes.

In our sample of 27 YSOs, $\sim$ 74% of them are resolved into multiple components or extended sources in high-resolution $JK_s$ images. To assess the physical properties of the YSOs, we have used the Online SED Model Fitter (Robitaille et al. 2007) to model SEDs of these YSOs and further analyzed in detail 22 YSOs that appear single or dominant within a group. We find good fits for Types I and II YSOs, though they show modest deviations between their observed SEDs and the models at 5.8 and 8.0$\mu$m, because the models do not include PAH emission. We have used a YSO with a *Spitzer* IRS observation to estimate the fraction of PAH emission in IRAC 3.6, 5.8, and 8.0 $\mu$m bands and modeled the SED with aromatic emission removed. That SED is well fit by the models, and comparisons between SEDs before and after PAH correction show that mass and total luminosity of the YSO is not significantly affected by including PAHs in models.

Some of the Type III YSOs show large deviations from the models at optical wavelengths. This is due to the modest angular resolution of the MCPS $UBVI$ catalog since the nebular line emission from small H II regions surrounding massive YSOs is not resolved from the point source and contributes to the broad-band photometry. We have also examined the effect of multiplicity (due to inadequate angular resolution) on inferring parameters of YSOs from SED fits by modeling a group of YSOs resolved in the VLT/NACO adaptive optics $JK_s$ images. We find that for a YSO of multiple sources at similar evolutionary stages, the integrated fluxes may result in up to 20% over-estimate in mass of the most massive component, but up to $\sim$ 40% under-estimate in the total mass of the system. For a YSO of sources at mixed evolutionary stages, the mid-IR luminosity is a good estimate for the system's total luminosity, but high-resolution optical and near-IR images are needed to separate main-sequence components from the YSO components.

YSO counterparts are found in one maser, three UCHIIs, and nine candidate HAeBe stars. The maser is associated with a Type I YSO and the majority of the HAeBe stars correspond to Type II and III YSOs, supporting the evolutionary sequence of our empirical classification. The maser has IRS spectral features similar to the "P" group classification used in Seale et al. (2009), while the three UCHIIs are similar to the "PE" group. Masers are typically associated with YSOs less evolved than UCHIIs, supporting the proposed spectral evolutionary sequence that YSOs with the "PE" spectral type are more evolved than those with the "P" spectral type. We have further found that for YSOs associated with ultracompact H II regions, (proto) stellar masses determined from SED model fits agree well with those estimated from the ionization requirements of the H II regions. Using the SED

model fits, we find at least 9 O-type YSOs in N 159.

N 159 encompasses three molecular concentrations with different star formation histories and intensities. O-type YSOs are found in the two GMCs that are associated with ionized gas, i.e., where massive stars have formed a few Myr ago, while no O-type YSOs are found in the third GMC that shows no signs of massive star formation in the optical and near-IR wavelengths. This result is similar to that seen in YSOs in the three GMCs in N 44 (Paper I), indicating that energy feedback plays a role in the formation of massive YSOs. However it remains unclear whether the less active GMCs will form massive stars later. Although the uncertainties in $\Delta V$ are large, the GMC N 159-W does have the smallest $\Delta V$ and $M_{\rm vir}/M_{\rm lum}$ ratio and also contains the largest number and most concentrated distribution of YSOs, consistent with the hypothesis that concentrated clusters are formed in a less gravitationally stable region. A smaller $M_{\rm vir}/M_{\rm lum}$ ratio is also found in the GMC N 44-C which has the highest number and the most concentrated distribution of YSOs.

To investigate whether star formation may be triggered or spontaneous in GMCs in N 159, we have performed a detailed comparison between the mid-IR YSO distribution and the distribution of already formed massive stars and their associated ionized gas. We find that the current star formation in the GMC N 159-E is likely to be triggered by H II regions expanding into the molecular cloud, while the massive YSOs in GMC N 159-W are more likely forming spontaneously.

Finally, we estimated star formation efficiencies and rates by counting the massive YSOs, and compared these rates to those inferred from integrated H$\alpha$ and 24 $\mu$m luminosities. We also compared with expected rates calculated from gas surface densities and using the Schmidt-Kennicutt extragalactic scaling relation. In GMCs with relatively high levels of activity, such as N159 -E and -W, the various measures are consistent. However, in more quiescent regions such as N 159-S and the giant molecular ridge which continues south from there, we find that star formation is distributed in relatively low luminosity regions and dominated by current (mid-IR detected) star formation, with a lack of massive main-sequence stars (representing few-Myr old activity). Star formation rates derived from YSO counting are higher than those predicted by total H$\alpha$ and 24 $\mu$m luminosities, and both are lower than would be implied by the total gas surface density. This discrepancy can be explained if the star formation sites are poor clusters which do not fully sample the stellar mass function (so their mass-to-light ratios are elevated). Alternatively, the youngest and most embedded still accreting massive protostars have elevated mass-to-light ratios due to late spectral type pre-main-sequence photospheres and possible having not yet accreted their final mass. Either possibility indicates unusual conditions in N 159-S and a breakdown of the scaling laws determined by averaging over kiloparsec scales in galaxies. Detailed studies such as this of

archival *Spitzer* data, soon to be complemented by detailed molecular gas properties obtained with ALMA, are revealing the full complexity of extragalactic star formation.

We thank the anonymous referee for the careful reading of the manuscript to improve the paper. We also thank Tony Wong for providing the MAGMA CO map. This work is supported through NASA grants JPL 1282653 and 1288328. R. A. G. and J. P. S. acknowledge supports from JPL grant 1316421 and NSF grant AST 08-07323. M. M. acknowledges support in part from *Spitzer* grant 1275598 and NASA grant NAG5-12595. This study made use of data products of the Two Micron All Sky Survey, which is a joint project of the University of Massachusetts and the Infrared Processing and Analysis Center/California Institute of Technology, funded by the National Aeronautics and the Space Administration and the National Science Foundation.

## REFERENCES

Allen, L. E., et al. 2004, ApJS, 154, 363

Bica, E., Claria, J. J., Dottori, H., Santos, Jr., J. F. C., & Piatti, A. E. 1996, ApJS, 102, 57

Bigiel, F., et al. 2008, AJ, 136, 2846

Blum, R. D., et al. 2006, AJ, 132, 2034

Bolatto, A. D., Leroy, A. K., Rosolowsky, E., Walter, F., & Blitz, L. 2008, ApJ, 686, 948

Bonnell, I. A., Bate, M. R., & Vine, S. G. 2003, MNRAS, 343, 413

Calzetti, D., et al. 2007, ApJ, 666, 870

Caplan, J., & Deharveng, L. 1986, A&A, 155, 297

Chen, C.-H. R., Chu, Y.-H., Gruendl, R. A., Gordon, K. D., & Heitsch, F. 2009, ApJ, 695, 511

Chu, Y.-H., Kennicutt, R. C., Snowden, S. L., Smith, R. C., Williams, R. M., & Bomans, D. J. 1997, PASP, 109, 554

Churchwell, E. 2002, ARA&A, 40, 27

Cowley, A. P., Schmidtke, P. C., Anderson, A. L., & McGrath, T. K. 1995, PASP, 107, 145

Deharveng, L., & Caplan, J. 1992, A&A, 259, 480

Desai, K. M., et al. 2010, ApJ, in press (ArXiv e-prints1006.3344)

Dickel, J. R., McIntyre, V. J., Gruendl, R. A., & Milne, D. K. 2005, AJ, 129, 790

Draine, B. T., & Li, A. 2007, ApJ, 657, 810

Ellingsen, S. P., Voronkov, M. A., Cragg, D. M., Sobolev, A. M., Breen, S. L., & Godfrey, P. D. 2007, in IAU Symposium, Vol. 242, IAU Symposium, ed. J. M. Chapman & W. A. Baan, 213–217

Fariña, C., Bosch, G. L., Morrell, N. I., Barbá, R. H., & Walborn, N. R. 2009, AJ, 138, 510

Fazio, G. G., et al. 2004, ApJS, 154, 10

Feast, M. 1999, in IAU Symp. 190: New Views of the Magellanic Clouds, ed. Y.-H. Chu, N. Suntzeff, J. Hesser, & D. Bohlender, 542

Fleener, C. E., Payne, J. T., Chu, Y., Chen, C., & Gruendl, R. A. 2010, AJ, 139, 158

Forbrich, J., Lada, C. J., Muench, A. A., Alves, J., & Lombardi, M. 2009, ApJ, 704, 292

Franco, J., Kurtz, S. E., García-Segura, G., & Hofner, P. 2000, Ap&SS, 272, 169

Fukui, Y., et al. 2008, ApJS, 178, 56

Gatley, I., Becklin, E. E., Hyland, A. R., & Jones, T. J. 1981, MNRAS, 197, 17P

Gorjian, V., et al. 2004, ApJS, 154, 275

Groenewegen, M. A. T. 2006, A&A, 448, 181

Gruendl, R. A., & Chu, Y. 2009, ApJS, 184, 172

Henize, K. G. 1956, ApJS, 2, 315

Heydari-Malayeri, M., Rosa, M. R., Charmandaris, V., Deharveng, L., & Zinnecker, H. 1999, A&A, 352, 665

Hillenbrand, L. A., Strom, S. E., Vrba, F. J., & Keene, J. 1992, ApJ, 397, 613

Huff, E. M., & Stahler, S. W. 2007, ApJ, 666, 281

Hughes, A., et al. 2010, MNRAS, 873

Hunt, M. R., & Whiteoak, J. B. 1994, Proceedings of the Astronomical Society of Australia, 11, 68

Indebetouw, R., Johnson, K. E., & Conti, P. 2004, AJ, 128, 2206

Indebetouw, R., et al. 2005, ApJ, 619, 931

—. 2008, AJ, 136, 1442

Johansson, L. E. B., et al. 1998, A&A, 331, 857

Jones, T. J., Woodward, C. E., Boyer, M. L., Gehrz, R. D., & Polomski, E. 2005, ApJ, 620, 731

Kato, D., et al. 2007, PASJ, 59, 615

Kennicutt, R. C., et al. 2009, ApJ, 703, 1672

Kennicutt, Jr., R. C. 1989, ApJ, 344, 685

—. 1998, ApJ, 498, 541

Kim, S., Staveley-Smith, L., Dopita, M. A., Sault, R. J., Freeman, K. C., Lee, Y., & Chu, Y. 2003, ApJS, 148, 473

Klessen, R. S., Burkert, A., & Bate, M. R. 1998, ApJ, 501, L205

Koornneef, J. 1983, A&A, 128, 84

Krumholz, M. R., McKee, C. F., & Tumlinson, J. 2009, ApJ, 699, 850

Lazendic, J. S., Whiteoak, J. B., Klamer, I., Harbison, P. D., & Kuiper, T. B. H. 2002, MNRAS, 331, 969

Leroy, A. K., et al. 2008, AJ, 136, 2782

Li, A., & Draine, B. T. 2001, ApJ, 554, 778

—. 2002, ApJ, 576, 762

Lucke, P. B., & Hodge, P. W. 1970, AJ, 75, 171

Massey, P. 1985, PASP, 97, 5

Meixner, M., et al. 2006, AJ, 132, 2268

Mizuno, N., et al. 2001, PASJ, 53, 971

Nakajima, Y., et al. 2005, AJ, 129, 776

Ott, J., et al. 2008, PASA, 25, 129

Pineda, J. L., Ott, J., Klein, U., Wong, T., Muller, E., & Hughes, A. 2009, ApJ, 703, 736

Pomarès, M., et al. 2009, A&A, 494, 987

Pottasch, S. R. 1993, in Infrared Astronomy, ed. A. Mampaso, M. Prieto, & F. Sanchez, 63

Rieke, G. H., et al. 2004, ApJS, 154, 25

Robitaille, T. P., Whitney, B. A., Indebetouw, R., & Wood, K. 2007, ApJS, 169, 328

Robitaille, T. P., Whitney, B. A., Indebetouw, R., Wood, K., & Denzmore, P. 2006, ApJS, 167, 256

Schaerer, D., & de Koter, A. 1997, A&A, 322, 598

Schaerer, D., Meynet, G., Maeder, A., & Schaller, G. 1993, A&AS, 98, 523

Schmidt-Kaler, T. 1982, in Landolt-Börnstein New Series, Group 6, Volume 2b, Stars and Star Clusters, ed. K. Schaifers & H. H. Voigt (Berlin: Springer)

Seale, J. P., et al. 2009, ApJ, 699, 150

Seward, F. D., Williams, R. M., Chu, Y., Gruendl, R. A., & Dickel, J. R. 2010, AJ, 140, 177

Simon, J. D., et al. 2007, ApJ, 669, 327

Skrutskie, M. F., et al. 2006, AJ, 131, 1163

Smith, R. C., & The MCELS Team. 1999, in IAU Symp. 190: New Views of the Magellanic Clouds, ed. Y.-H. Chu, N. Suntzeff, J. Hesser, & D. Bohlender, 28

Testor, G., Lemaire, J. L., Field, D., & Diana, S. 2006, A&A, 453, 517

Testor, G., Lemaire, J. L., Kristensen, L. E., Field, D., & Diana, S. 2007, A&A, 469, 459

Vaidya, K., Chu, Y., Gruendl, R. A., Chen, C., & Looney, L. W. 2009, ApJ, 707, 1417

van der Bliek, N. S., et al. 2004, Proc. SPIE, 5492, 1582

Vanhala, H. A. T., & Cameron, A. G. W. 1998, ApJ, 508, 291

Walter, F., et al. 2008, AJ, 136, 2563

Whitney, B. A., Indebetouw, R., Bjorkman, J. E., & Wood, K. 2004, ApJ, 617, 1177

Whitney, B. A., Wood, K., Bjorkman, J. E., & Wolff, M. J. 2003, ApJ, 591, 1049

Whitney, B. A., et al. 2008, AJ, 136, 18

Williams, R. M., Petre, R., Chu, Y.-H., & Chen, C.-H. R. 2000, ApJ, 536, L27

Wood, K., Whitney, B. A., Robitaille, T., & Draine, B. T. 2008, ApJ, 688, 1118

Yorke, H. W., & Sonnhalter, C. 2002, ApJ, 569, 846

Zaritsky, D., Harris, J., Thompson, I. B., & Grebel, E. K. 2004, AJ, 128, 1606

Zavagno, A., Pomarès, M., Deharveng, L., Hosokawa, T., Russeil, D., & Caplan, J. 2007, A&A, 472, 835

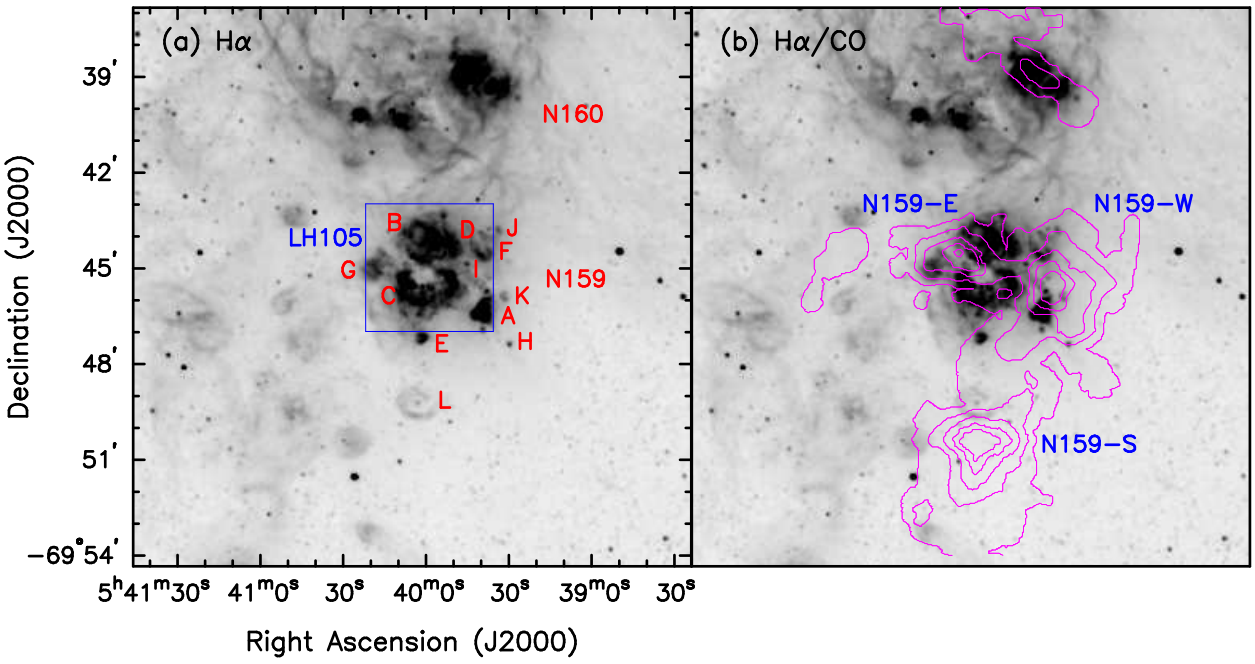


Fig. 1.— MCELS H$\alpha$ images of N 159. (a) MCELS H$\alpha$ image of N 159, showing the nebular components A-L defined by Henize (1956) and the OB association LH105 cataloged by Lucke & Hodge (1970). (b) CO contours overlaid and three GMCs near CO peaks cataloged by Johansson et al. (1998) labeled on the MCELS H$\alpha$ image.

Fig. 2.— IRAC and MIPS images of N 159. (a) 3.6 $\mu$m image showing stars and modest PAH emission, with OB association LH105 labeled; (b) 8.0 $\mu$m image showing PAH and dust emissions, (c) 24 $\mu$m image showing dust emission and overlaid with CO contours from Johansson et al. (1998) , and (d) color composite of 3.6, 8.0, and 24 $\mu$m images. Dust shrouded objects, e.g., YSOs and AGB stars, appear red.

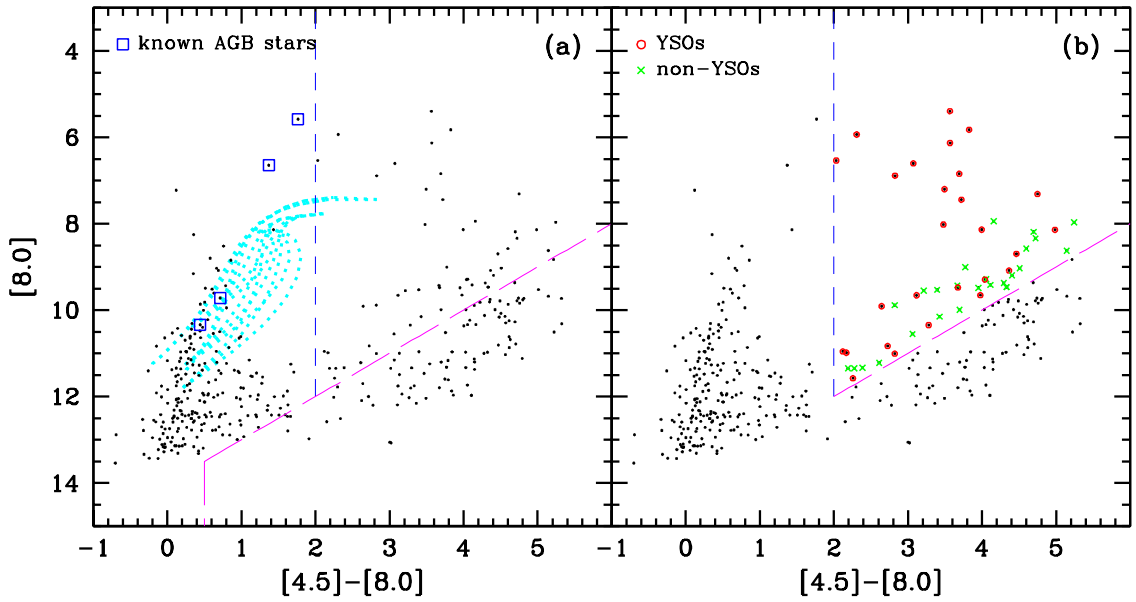


Fig. 3.— (a) [8.0] vs. [4.5]−[8.0] CMD of all sources detected in N 159. Known AGB stars are marked with open blue squares and expected loci from AGB stellar models (Groenewegen 2006) with filled cyan squares. The criterion to exclude normal and AGB stars is shown in short-dashed lines and that to exclude background galaxies in long-dashed lines. (b) 52 YSO candidates are found in the upper right wedge that has the minimum contamination from stars and background galaxies. These candidates have been through detail examination using multi-wavelength images and SEDs. Candidates that are most likely YSOs are marked with red open circles and non-YSOs with green crosses.

Fig. 4.— (a) 8 $\mu$m image of N 159 overlaid with MAGMA CO intensity contours (blue) in $n^2$ K km $s^{-1}$ (n=1,2,3,...) and marked with YSOs from three studies. 27 YSOs from this study are marked in the red circles, 5 YSOs from Jones et al. (2005) are marked in yellow triangles and labeled with numbers 1-5, and 4 YSOs from Whitney et al. (2008) are marked in cyan boxes and labeled with numbers 1-4. The FOV of the Jones et al. (2005) study is smaller and marked with dashed yellow lines. (b) YSOs in N 159 from this study, Jones et al. (2005, abbreviated as J05 in the figure), and Whitney et al. (2008, abbreviated as W08 in the figure) marked on a [8.0] vs. ([4.5]−[8.0]) CMD. Symbols are the same as in (a) and numbers are attached with an extra letter of J or W to separate samples from the Jones et al. (2005) and Whitney et al. (2008) studies.

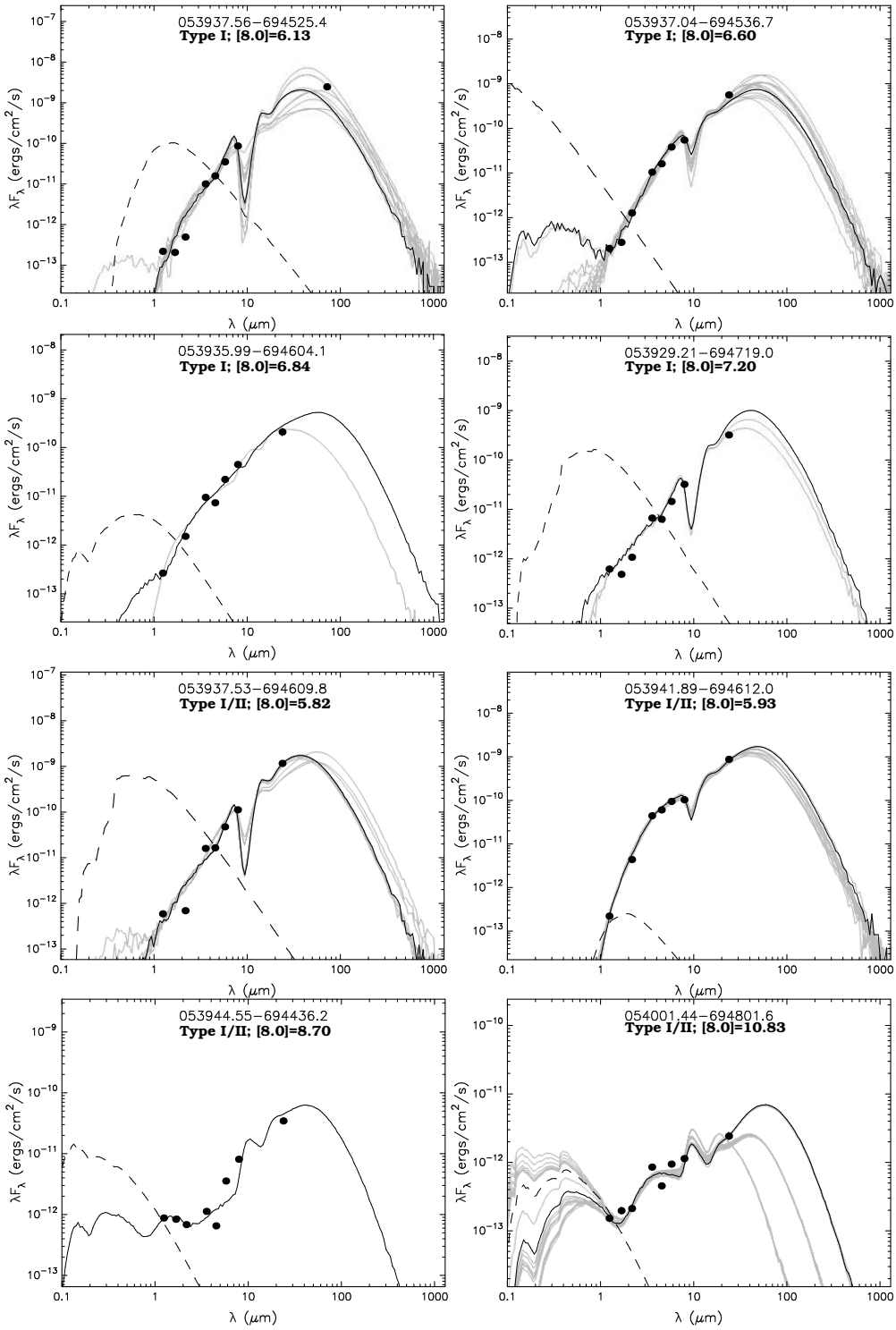


Fig. 5.— SEDs of 27 YSOs analyzed in this study. Filled circles are the flux values converted from magnitudes listed in Table 4. The source name, Type from our empirical classification, and [8.0] mag are labeled at the top of the plot. Triangles are upper limits. Error bars are shown if larger than the data points. The solid black line shows the best-fit model, and the dashed black line illustrates the radiation from the central star reddened by the best-fit $A_V$. The gray lines show all acceptable models.

.

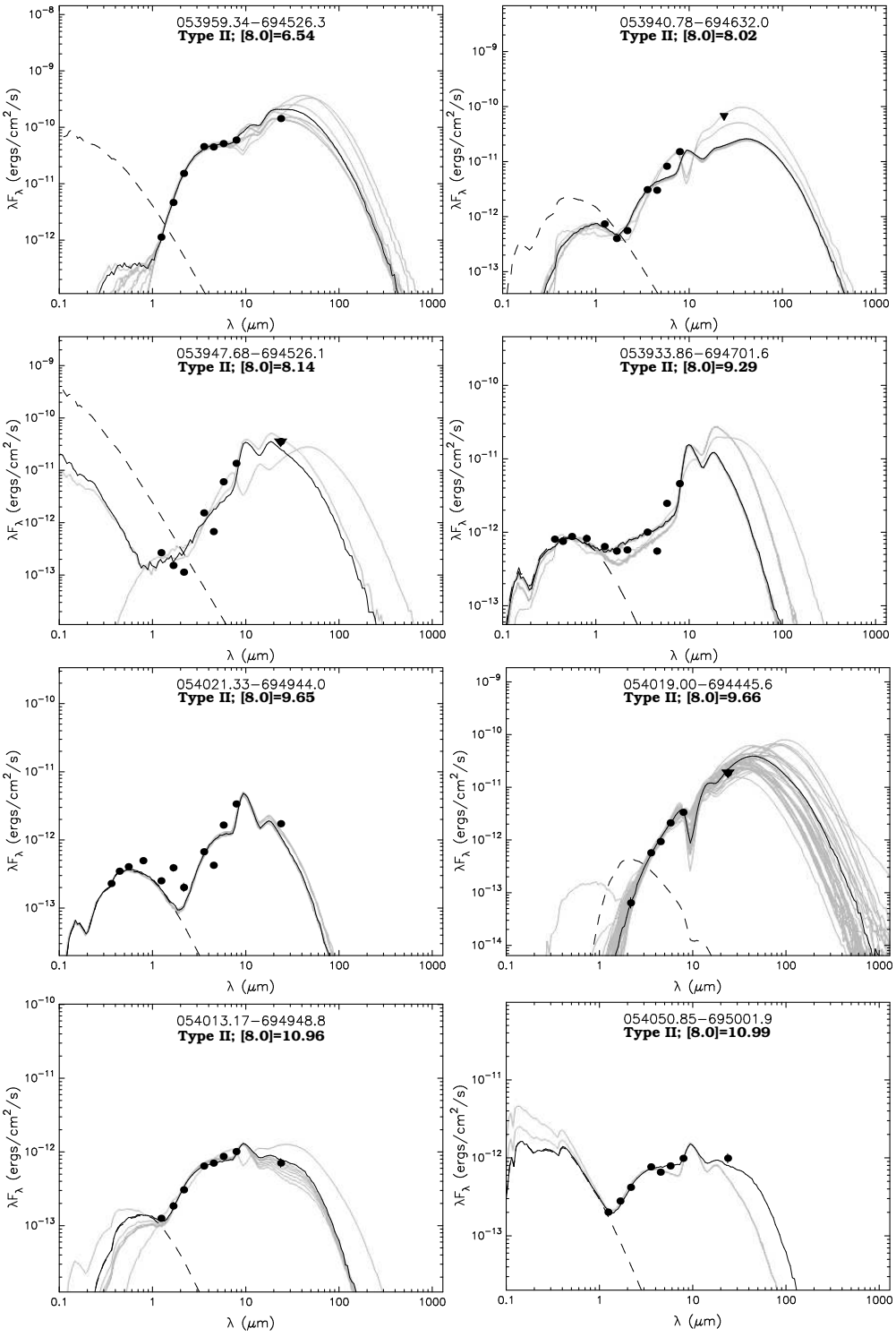


Figure 5 — Continued.

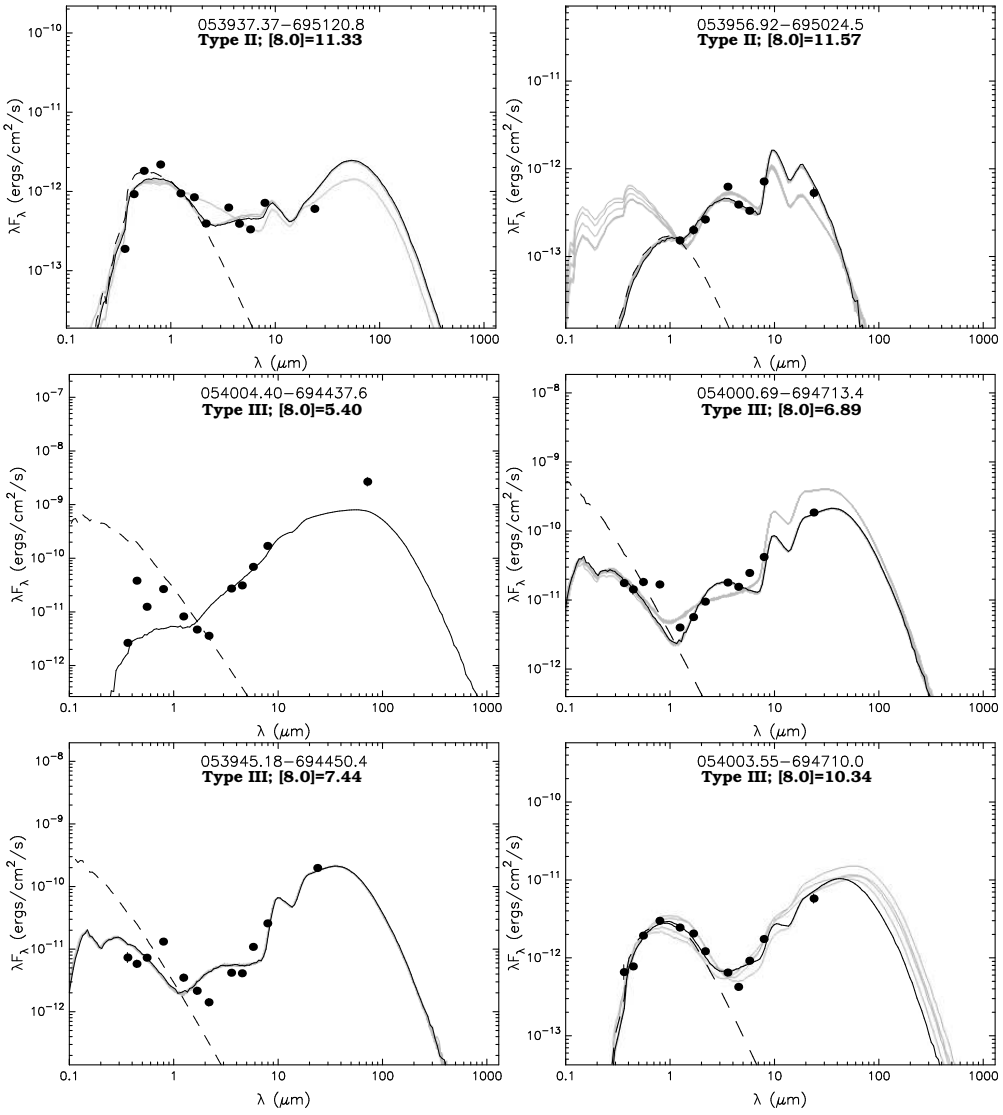


Figure 5 — Continued.

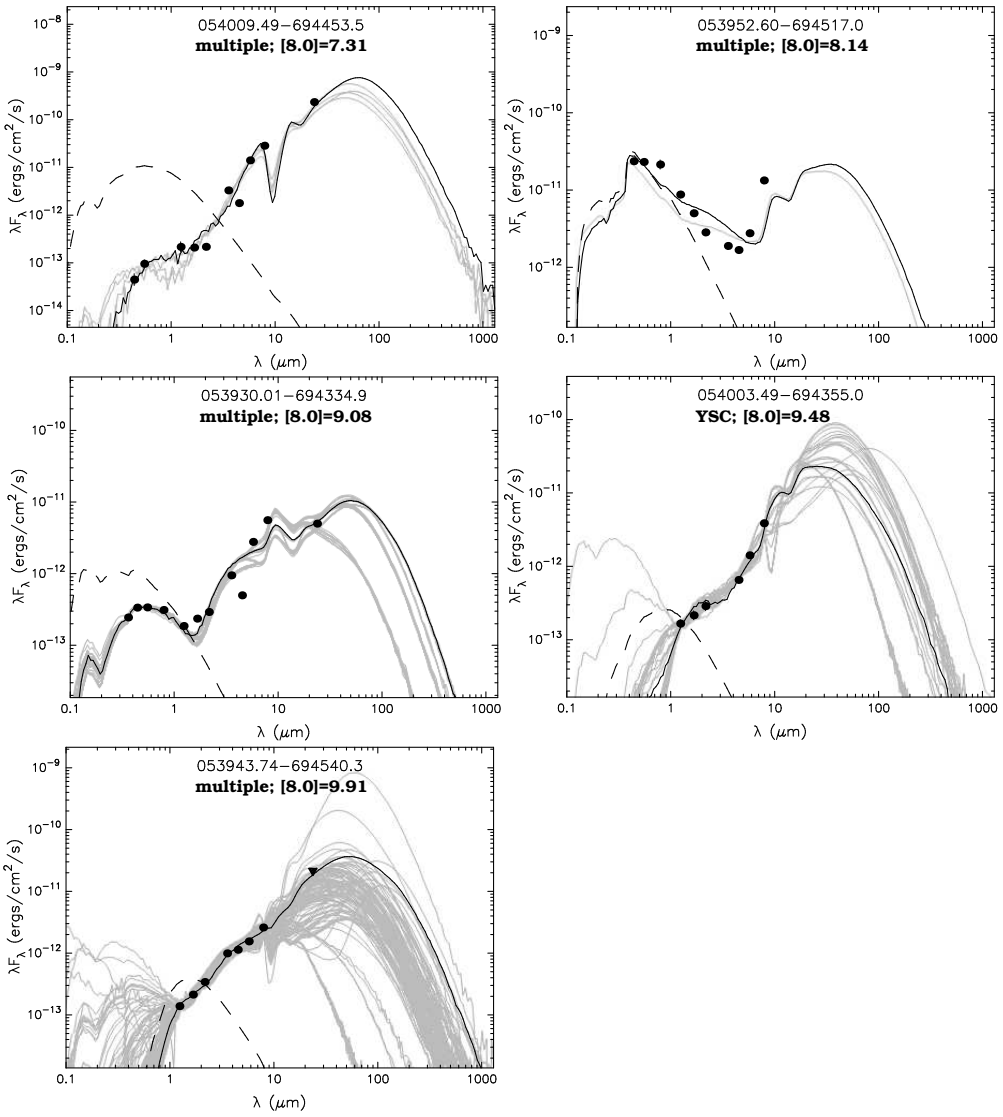


Figure 5 — Continued.

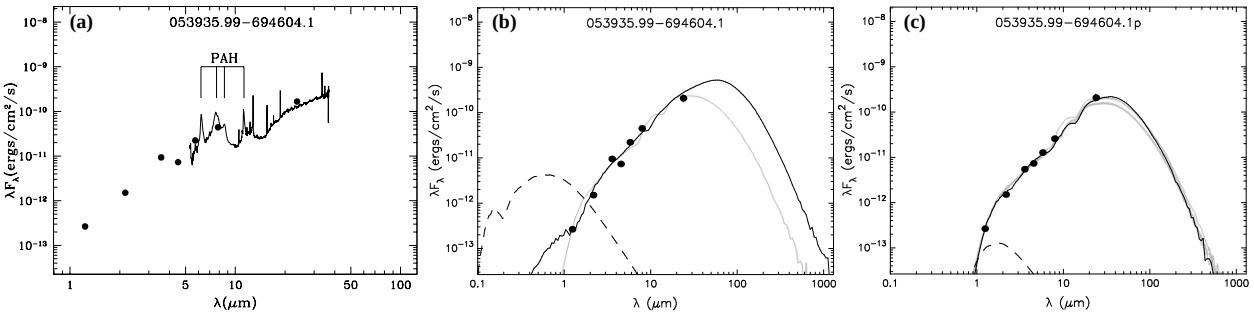


Fig. 6.— (a)Multi-wavelength SED (filled circles, this study) and IRS spectrum (solid line, Seale et al. 2009) of YSO 053935.99−694604.1. PAH features at 6.2, 7.7, 8.6, and 11.3 $\mu$m are labeled in the IRS spectrum. (b) and (c) Model fits to the SED before and after correcting contribution of PAH emission. Symbols in (b) and (c) are the same as in Figure 5.

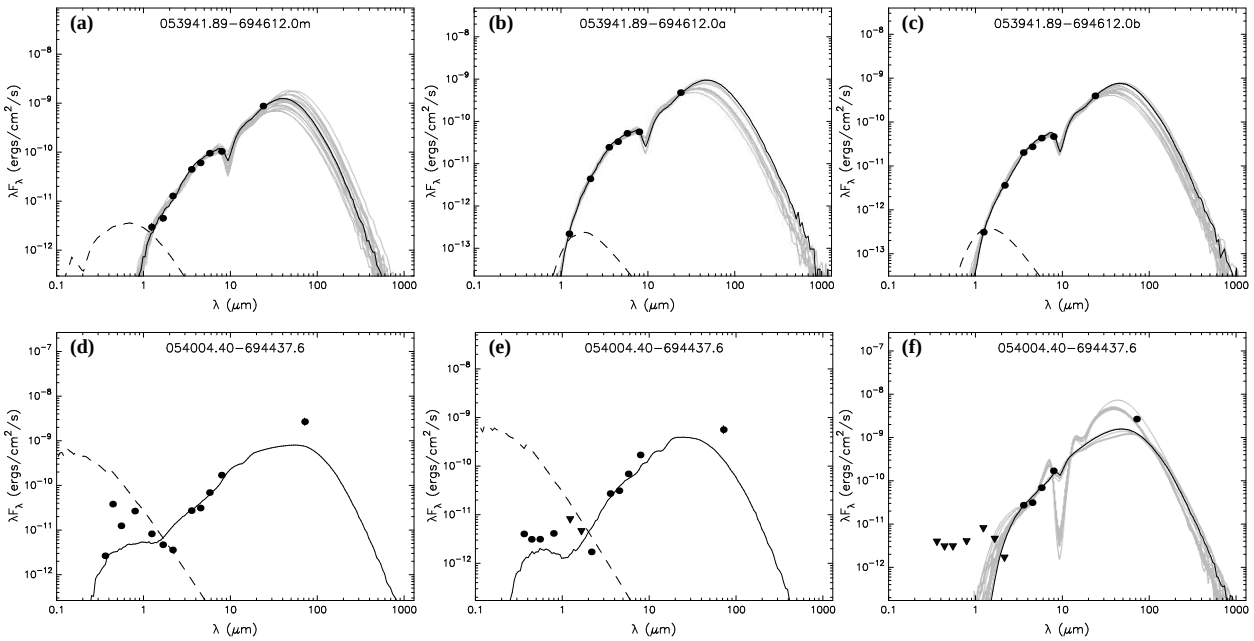


Fig. 7.— Upper panel: model fits to a multiple system with sources at similar evolutionary stage. (a) SED of 053941.89−694612.0 from integrated fluxes of the system. (b,c) SEDs of the two brightest YSOs, labeled as a and b respectively in the figure, from their NACO $K_s$ luminosities and proportioned IRAC and MIPS fluxes (according to the $K_s$ luminosity). Lower panel: model fits to a multiple system with sources at different different evolutionary stages. Optical and near-IR segments of SEDs of YSO 054004.40−694437.6 are constructed from (d) $UBVI$ from MCPS and $JHK_s$ from IRSF, (e) high-resolution $UbyI$ from *HST* and $K_s$ from VLT/NACO, and (f) optical and near-IR fluxes used only as upper limits. See text for detail. Symbols are the same as in Figure 5.

Fig. 8.— (a) 8 $\mu$m image of N 159 overlaid with MAGMA CO intensity contours (blue) in n$^2$ K km s$^{-1}$ (n=1,2,3,...). YSOs at different evolutionary stages are marked as follows: red circle – Type I and I/II, green circle – Type II and II/III, and blue circle – Type III. Known maser and UCHIIs are marked with additional triangle and boxes, respectively (Lazendic et al. 2002; Indebetouw et al. 2004). Candidate HAeBe stars from Nakajima et al. (2005) are marked in orange dots. Candidate HAeBe stars in common with YSOs are labeled with positive numbers, and those in common with non-YSO red sources (yellow pluses) are labeled with negative numbers. (b) $J-H$ vs. $H-K_s$ CMD of all sources detected in all three $JHK_s$ bands in N 159. YSOs and non-YSO red sources in common with candidate HAeBe stars are labeled with numbers as in (a) and marked with additional red circles and yellow crosses, respectively. Dashed magenta lines indicate the criterion used to select candidate HAeBe stars in the Nakajima et al. (2005) study. (c) same as in (b) for the $K$ vs. $J-K_s$ CMD.

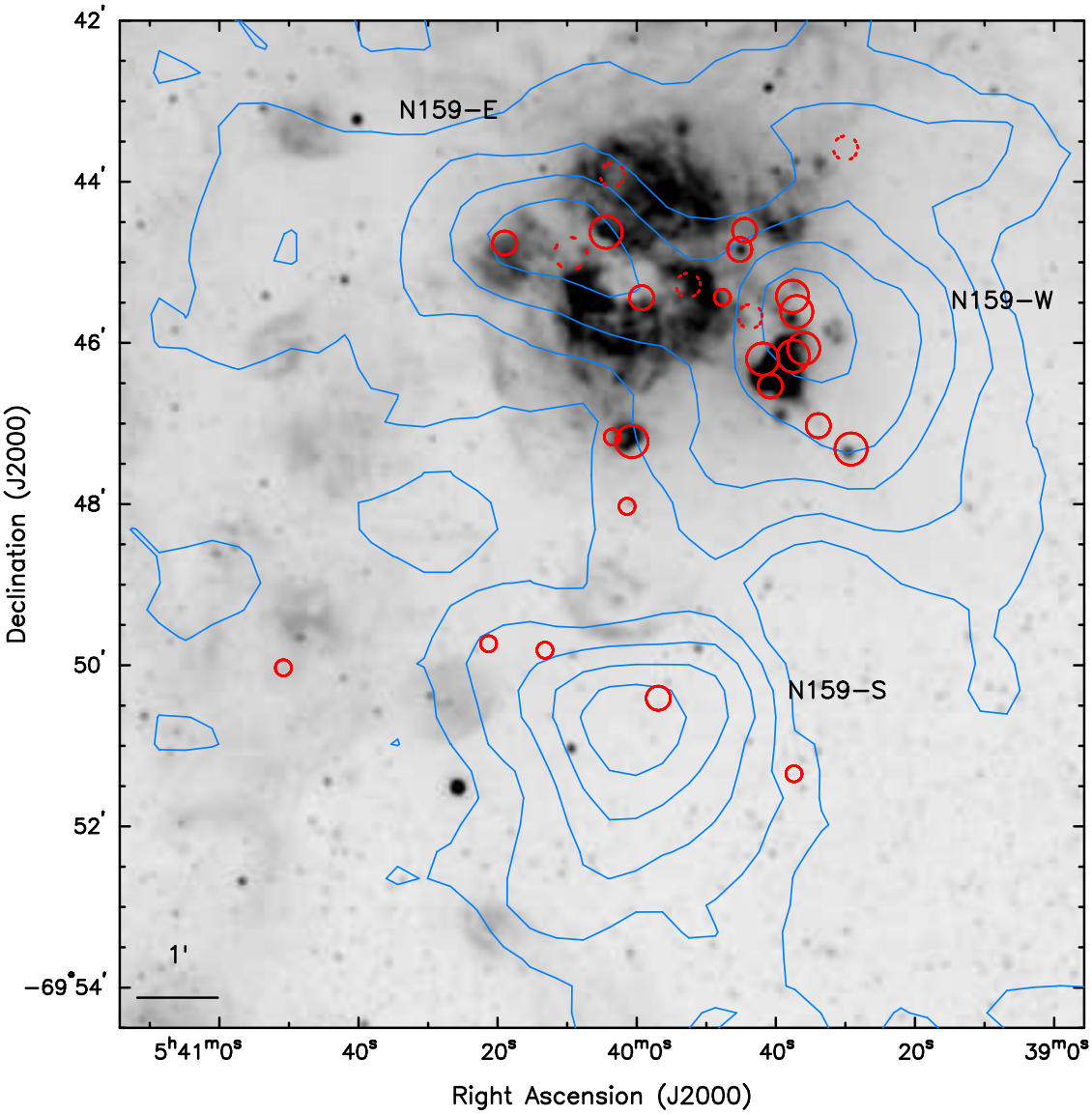


Fig. 9.— Distribution of YSOs with respect to interstellar environments of N 159. The H$\alpha$ image of N 159 is shown in grey scale, overlaid with MAGMA CO intensity contours (blue) in n$^2$ K km s$^{-1}$ (n=1,2,3,...). YSOs with different mass estimates are marked with different symbols: O-type, i.e., $\bar{M}_\star \geq 17\ M_\odot$, as large red open circles; early-B type, i.e., $17\ M_\odot > \bar{M}_\star \geq 8\ M_\odot$, as medium red open circles; and B-type, i.e., $\bar{M}_\star < 8\ M_\odot$, as small red open circles. YSOs that appear single or are clearly the dominant source with the IRAC PSF are shown in solid-line circles, while YSOs that are multiple and have larger uncertainties in mass estimates are in dotted-line circles.

Fig. 10.— (a) MOSAIC H$\alpha$ image of N 159 superbubble overlaid with 3 cm contours (yellow). The position and size of the SNR 0540−697 are marked in dashed cyan line. YSOs are marked in the same symbols as Figure 9. Spectroscopically identified massive stars (Fariña et al. 2009) are marked with triangles in three sizes to show different evolutionary stages: large – young phase including O4-5 V-I and O Vz, medium – middle-aged phase including O6-9 V-I and B0 I, and small – evolved phase including B0-2 V-III and B1-8 I. (b) Extinction map overlaid with MAGMA CO intensity contours (magenta). YSOs and spectroscopically identified massive stars are marked in the same symbols as (a). Candidate OB stars from Nakajima et al. (2005) are marked in green squares.

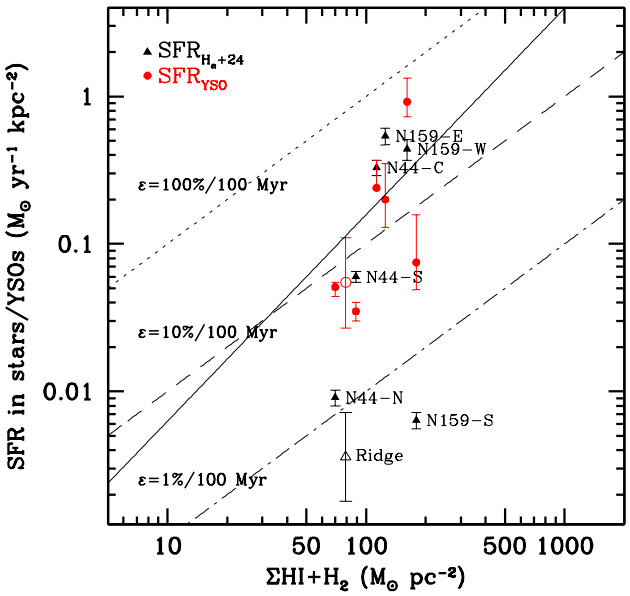


Fig. 11.— Relation between the SFR per unit area and gas density for six GMCs in N 44 and N 159. Each GMC has two estimated SFRs using different tracers, $SFR_{H\alpha+24}$ (filled triangles and GMC name labeled) and $SFR_{YSO}$ (filled circles). For comparison, SFRs estimated in the molecular ridge (Indebetouw et al. 2008) are also plotted, i.e., $SFR_{H\alpha+24}$ in open triangle and $SFR_{YSO}$ in open circle. The solid line is the S-K relation, and the dotted, dashed, dashed-dotted lines correspond to constant SFRs per unit gas mass, in units of 1%, 10%, and 100% per 100 Myr, commonly used in estimating SFRs of a galaxy (Kennicutt 1998). GMCs without prominent H II regions, i.e., N 44-N, N 159-S, and the molecular ridge, have $SFR_{H\alpha+24}$ 11–56 times smaller than expected from the S-K relation, but their $SFR_{YSO}$ are in better agreement with the S-K relation.

Table 1. Archival *Spitzer* Observations of N 159

| Program ID | Principal Investigator | Observation Parameters IRAC | MIPS |
|---|---|---|---|
| 124 | Gehrz | $10 \times 12^{a}$ s | |
| 20203 | Meixner | $4 \times 12^{a}$ s | 2× Fast Scan |

[a]Observations used high dynamic range mode and had complementary exposures.

Table 2. Archival *HST* WFPC2/ACS Observations of Fields in N 159

| R.A. (J2000) | Decl. (J2000) | Program ID/PI | Detector/Filter[a] | Exp. Time (s) |
|---|---|---|---|---|
| 05 39 10.5 | −69 41 52.1 | 9480/Rhodes | ACS/F775W | 1200.0 |
| 05 40 12.8 | −69 44 29.3 | 06535/Heydari-Malayeri | WFPC2/F300W | 51.2 |
| | | | WFPC2/F410M | 172.0 |
| | | | WFPC2/F467M | 139.2 |
| | | | WFPC2/F469N | 1292.0 |
| | | | WFPC2/F487N | 1272.0 |
| | | | WFPC2/F502N | 984.0 |
| | | | WFPC2/F547M | 34.4 |
| | | | WFPC2/F656N | 1280.0 |
| | | | WFPC2/F814W | 21.6 |
| 05 40 14.3 | −69 50 06.8 | 09827/Bianchi | WFPC2/F170W | 240.0 |
| | | | WFPC2/F225W | 200.0 |
| | | | WFPC2/F336W | 40.0 |
| | | | WFPC2/F439W | 40.0 |
| | | | WFPC2/F555W | 20.0 |
| 05 40 50.3 | −69 55 10.2 | 9827/Bianchi | ACS/F435W | 130.0 |
| | | | ACS/F555W | 100.0 |
| | | | ACS/F658N | 600.0 |
| | | | ACS/F814W | 80.0 |

[a]F330W: Wide $U$; F336W: WFPC2 $U$; F410M: Strömgren $v$; F435W: Johnson $B$; F439W: WFPC2 $B$; F467M: Strömgren $b$; F469N: He II; F487N: H$\beta$; F502N: [O III]; F547M: Strömgren $y$; F555W: Johnson $V$; F656N: H$\alpha$; F658N: H$\alpha$; F673N: [S II]; F675W: WFPC2 $R$; F775W: SDSS $i$; F814W: Broad $I$.

Table 3. Parameters for IRAC and MIPS Photometric Measurements

| Band | Aperture Radius (″) | Background Annulus (″) | Aperture Correction Factor | Zero-Mag. Flux (Jy) |
|---|---|---|---|---|
| IRAC 3.6 $\mu$m | 3.6 | 3.6-8.4 | 1.124 | 277.5 |
| 4.5 $\mu$m | 3.6 | 3.6-8.4 | 1.127 | 179.5 |
| 5.8 $\mu$m | 3.6 | 3.6-8.4 | 1.143 | 116.6 |
| 8.0 $\mu$m | 3.6 | 3.6-8.4 | 1.234 | 63.1 |
| MIPS 24 $\mu$m | 6 | 20-32 | 1.699 | 7.14 |
| 70 $\mu$m | 16 | 39-65 | 2.087 | 0.775 |

Table 4. Multi-wavelength Photometry of YSO Candidates Selected from CMD Criteria

| Name (1) | No (2) | [3.6] (3) | [4.5] (4) | [5.8] (5) | [8.0] (6) | [24] (7) | [70] (8) | Class. (9) | Remarks (10) |
|---|---|---|---|---|---|---|---|---|---|
| 053921.21-694409.4 | 51 | 13.76 0.01 | 13.54 0.01 | 12.54 0.04 | 11.35 0.14 | ··· ··· | ··· ··· | S in DR | |
| 053929.21-694719.0 | 9 | 11.38 0.01 | 10.69 0.01 | 9.05 0.02 | 7.20 0.02 | 1.12 0.01 | ··· ··· | I | ext |
| 053930.01-694334.9 | 24 | 13.48 0.02 | 13.45 0.02 | 10.85 0.03 | 9.08 0.03 | 5.64 0.05 | ··· ··· | II | mul |
| 053932.52-694357.4 | 17 | 12.82 0.03 | 12.88 0.03 | 9.84 0.03 | 8.19 0.03 | ··· ··· | ··· ··· | D | |
| 053932.73-694344.3 | 29 | 13.82 0.05 | 13.53 0.07 | 11.14 0.06 | 9.42 0.08 | ··· ··· | ··· ··· | D peak | |
| 053933.86-694701.6 | 27 | 13.42 0.01 | 13.33 0.01 | 10.97 0.01 | 9.29 0.02 | ··· ··· | ··· ··· | II | |
| 053935.99-694604.1 | 7 | 10.99 0.01 | 10.53 0.01 | 8.59 0.01 | 6.84 0.01 | 1.60 0.10 | ··· ··· | I | mul |
| 053937.04-694536.7 | 6 | 10.87 0.01 | 9.68 0.01 | 8.01 0.01 | 6.60 0.01 | 0.51 0.01 | ··· ··· | I | mul |
| 053937.37-695120.8 | 49 | 13.95 0.02 | 13.72 0.02 | 13.14 0.07 | 11.33 0.04 | 7.94 0.07 | ··· ··· | II | ext |
| 053937.53-694609.8 | 2 | 10.41 0.01 | 9.65 0.01 | 7.77 0.01 | 5.82 0.01 | -0.28 0.01 | ··· ··· | I/II | mul |
| 053937.56-694525.4 | 4 | 10.93 0.02 | 9.70 0.01 | 8.09 0.03 | 6.13 0.03 | ··· ··· | -4.70 0.20 | I | ext |
| 053938.09-694654.2 | 18 | 12.95 0.04 | 13.06 0.06 | 10.08 0.03 | 8.34 0.05 | ··· ··· | ··· ··· | S in DR | |
| 053938.80-694436.0 | 38 | 12.92 0.02 | 12.71 0.04 | 12.13 0.06 | 9.88 0.05 | ··· ··· | ··· ··· | S | LMC X-1 |
| 053939.10-694443.7 | 34 | 13.36 0.05 | 12.92 0.05 | 11.20 0.04 | 9.53 0.04 | ··· ··· | ··· ··· | D | |
| 053939.54-694400.2 | 19 | ··· ··· | 13.18 0.05 | 10.34 0.03 | 8.58 0.04 | ··· ··· | ··· ··· | D | |
| 053940.78-694632.0 | 14 | 12.21 0.02 | 11.49 0.02 | 9.66 0.02 | 8.02 0.02 | 2.81 99.9 | ··· ··· | II | |
| 053941.89-694612.0 | 3 | 9.32 0.01 | 8.24 0.01 | 7.00 0.01 | 5.93 0.01 | 0.04 0.01 | ··· ··· | I/II | mul |
| 053943.74-694540.3 | 39 | 13.43 0.01 | 12.55 0.01 | 11.48 0.04 | 9.91 0.05 | 4.06 99.9 | ··· ··· | III | mul |
| 053944.55-694436.2 | 21 | 13.31 0.04 | 13.16 0.03 | 10.57 0.04 | 8.70 0.04 | 3.55 0.05 | ··· ··· | I/II | |
| 053945.18-694450.4 | 11 | 11.88 0.01 | 11.16 0.01 | 9.36 0.01 | 7.44 0.01 | 1.65 0.01 | ··· ··· | III | ext |
| 053945.20-694508.1 | 22 | 13.05 0.05 | 12.78 0.03 | 10.72 0.06 | 9.00 0.06 | ··· ··· | ··· ··· | D | |
| 053945.21-694533.1 | 41 | 14.38 0.04 | 13.58 0.04 | ··· ··· | 10.15 0.05 | ··· ··· | ··· ··· | S in DR | |
| 053946.39-694435.5 | 20 | 13.26 0.04 | 13.77 0.07 | 10.35 0.03 | 8.62 0.03 | ··· ··· | ··· ··· | D | |
| 053947.68-694526.1 | 16 | 12.97 0.02 | 13.12 0.05 | 10.00 0.02 | 8.14 0.03 | 3.51 99.9 | ··· ··· | II | |
| 053948.25-694534.3 | 28 | 14.06 0.04 | 13.66 0.06 | 11.31 0.04 | 9.37 0.04 | ··· ··· | ··· ··· | D | |
| 053948.83-694416.7 | 23 | 13.33 0.03 | 13.54 0.03 | 10.85 0.03 | 9.03 0.03 | ··· ··· | ··· ··· | D peak | |
| 053949.26-694407.5 | 31 | 14.00 0.07 | 13.80 0.09 | 11.24 0.04 | 9.47 0.05 | ··· ··· | ··· ··· | D | |
| 053950.29-694545.4 | 40 | 14.22 0.04 | 13.69 0.10 | 11.74 0.07 | 9.99 0.08 | ··· ··· | ··· ··· | D | |
| 053952.39-694518.3 | 12 | ··· ··· | 12.10 0.03 | 10.74 0.04 | 7.94 0.03 | ··· ··· | ··· ··· | D | |
| 053952.60-694517.0 | 15 | 12.73 0.02 | 12.13 0.04 | 10.85 0.04 | 8.14 0.03 | ··· ··· | ··· ··· | III | mul |
| 053956.62-694439.1 | 30 | 13.55 0.03 | 13.10 0.03 | 11.28 0.03 | 9.43 0.03 | ··· ··· | ··· ··· | D | |
| 053956.92-695024.5 | 52 | 14.62 0.01 | 13.83 0.01 | 13.49 0.04 | 11.57 0.03 | 8.08 0.11 | ··· ··· | II | mul |
| 053959.34-694526.3 | 5 | 9.29 0.01 | 8.57 0.01 | 7.67 0.01 | 6.54 0.01 | 2.00 0.01 | ··· ··· | II | ext |

Table 4—Continued

| Name (1) | No (2) | [3.6] (3) | [4.5] (4) | [5.8] (5) | [8.0] (6) | [24] (7) | [70] (8) | Class. (9) | Remarks (10) |
|---|---|---|---|---|---|---|---|---|---|
| 054000.69-694713.4 | 8 | 10.29 0.01 | 9.71 0.01 | 8.48 0.01 | 6.89 0.01 | 1.72 0.01 | ··· ··· | III | ext |
| 054001.44-694801.6 | 44 | 13.61 0.02 | 13.55 0.02 | 12.01 0.05 | 10.83 0.08 | 6.43 0.07 | ··· ··· | I/II | |
| 054003.49-694355.0 | 32 | ··· ··· | 13.15 0.02 | 11.58 0.08 | 9.48 0.05 | ··· ··· | ··· ··· | YSC | |
| 054003.55-694710.0 | 42 | 13.89 0.03 | 13.62 0.05 | 12.05 0.05 | 10.34 0.06 | 5.48 0.15 | ··· ··· | III | |
| 054004.13-694532.8 | 43 | 14.85 0.09 | 13.61 0.05 | 12.38 0.06 | 10.55 0.06 | ··· ··· | ··· ··· | S in DR | |
| 054004.40-694437.6 | 1 | 9.85 0.01 | 8.96 0.01 | 7.35 0.01 | 5.40 0.01 | ··· ··· | -4.79 0.20 | III | ext |
| 054005.91-694451.6 | 26 | 14.30 0.10 | 13.34 0.07 | ··· ··· | 9.28 0.05 | ··· ··· | ··· ··· | D | |
| 054006.85-694400.6 | 25 | 13.63 0.04 | 13.60 0.05 | 10.90 0.03 | 9.19 0.03 | ··· ··· | ··· ··· | D | |
| 054008.53-694530.6 | 35 | 13.58 0.06 | 12.76 0.07 | 11.93 0.11 | 9.55 0.06 | ··· ··· | ··· ··· | D | |
| 054009.49-694453.5 | 10 | 12.12 0.01 | 12.06 0.02 | 9.09 0.02 | 7.31 0.02 | 1.46 0.03 | ··· ··· | I/II | mul |
| 054011.47-694504.5 | 13 | 13.17 0.09 | 13.21 0.07 | 9.89 0.03 | 7.96 0.03 | ··· ··· | ··· ··· | D | |
| 054013.17-694948.8 | 45 | 13.91 0.01 | 13.07 0.01 | 12.10 0.02 | 10.96 0.04 | 7.77 0.12 | ··· ··· | II | |
| 054014.04-694454.8 | 33 | 13.81 0.03 | 13.43 0.04 | 11.38 0.03 | 9.48 0.05 | ··· ··· | ··· ··· | S in DR | |
| 054019.00-694445.6 | 37 | 14.05 0.04 | 12.77 0.02 | 11.13 0.03 | 9.66 0.04 | 4.22 99.9 | ··· ··· | II | ext |
| 054021.33-694944.0 | 36 | 13.87 0.02 | 13.63 0.03 | 11.40 0.02 | 9.65 0.03 | 6.80 0.06 | ··· ··· | II | mul |
| 054037.09-694521.5 | 48 | 14.05 0.01 | 13.83 0.01 | 13.75 0.05 | 11.22 0.01 | ··· ··· | ··· ··· | G | |
| 054044.66-694550.9 | 47 | 14.05 0.01 | 13.83 0.01 | 13.76 0.05 | 11.01 0.01 | 8.34 0.12 | ··· ··· | G | |
| 054046.29-694441.1 | 50 | 13.50 0.01 | 13.62 0.01 | 12.58 0.05 | 11.35 0.06 | ··· ··· | ··· ··· | S in DR | |
| 054050.85-695001.9 | 46 | 13.72 0.01 | 13.15 0.01 | 12.21 0.01 | 10.98 0.02 | 7.40 0.06 | ··· ··· | II | |

Note. — Column 1: source name. Column 2: Ranking of the brightness at 8 $\mu$m. Columns 3-8: photometric measurements in 3.6, 4.5, 5.8, 8.0, 24, and 70 $\mu$m bands in magnitudes. Measurements with uncertainties of 99.9 are the upper brightness limits as they include fluxes from neighbors or backgrounds. The uncertainties listed here are only errors in measurements and do not include errors in in flux calibration, i.e., 5% in 3.6, 4.5, 5.8, and 8.0 $\mu$m, 10% in 24 $\mu$m, and 20% in 70 $\mu$m. Thus, the total uncertainty of a flux is the quadratic sum of the measurement error and the calibration error. Columns 9 and 10: classification and remarks: D – diffuse emission, DR – dusty region, ext – extended source, G – background galaxy, I/II/III – Type I/II/III YSO, mul – multiple, S – star, YSC – young star cluster.

Table 5. Multi-wavelength Photometry of YSO Candidates Selected from CMD Criteria

| Name (1) | No (2) | $U$ (3) | $B$ (4) | $V$ (5) | $I$ (6) | $J$ (7) | $H$ (8) | $K_s$ (9) | Flag (10) | Class. (11) | Remarks (12) |
|---|---|---|---|---|---|---|---|---|---|---|---|
| 053921.21-694409.4 | 51 | ··· ··· | 21.88 0.22 | 21.17 0.20 | ··· ··· | 16.04 0.11 | 15.30 0.12 | 14.95 0.15 | 0 | S in DR | |
| 053929.21-694719.0 | 9 | ··· ··· | ··· ··· | ··· ··· | ··· ··· | 16.99 0.05 | 16.45 0.15 | 14.84 0.08 | 10 | I | ext |
| 053930.01-694334.9 | 24 | 19.45 0.10 | 19.77 0.06 | 19.41 0.06 | 18.67 0.08 | 18.29 0.06 | 17.23 0.07 | 16.25 0.05 | 10 | II | mul |
| 053932.52-694357.4 | 17 | ··· ··· | ··· ··· | ··· ··· | ··· ··· | ··· ··· | ··· ··· | ··· ··· | 0 | D | |
| 053932.73-694344.3 | 29 | ··· ··· | ··· ··· | ··· ··· | ··· ··· | ··· ··· | ··· ··· | ··· ··· | 0 | D peak | |
| 053933.86-694701.6 | 27 | 18.16 0.08 | 18.89 0.05 | 18.37 0.06 | 17.61 0.13 | 16.95 0.03 | 16.30 0.04 | 15.51 0.04 | 10 | II | |
| 053935.99-694604.1 | 7 | ··· ··· | ··· ··· | ··· ··· | ··· ··· | 17.91 0.10 | ··· ··· | 14.47 0.10 | 20 | I | mul |
| 053937.04-694536.7 | 6 | ··· ··· | ··· ··· | ··· ··· | ··· ··· | 18.19 0.09 | 17.04 0.15 | 14.65 0.05 | 10 | I | mul |
| 053937.37-695120.8 | 49 | ··· ··· | 19.77 0.05 | 18.71 0.05 | 17.64 0.05 | 16.53 0.05 | 15.85 0.09 | 15.93 0.11 | 10 | II | ext |
| 053937.53-694609.8 | 2 | ··· ··· | ··· ··· | ··· ··· | ··· ··· | 17.04 0.10 | ··· ··· | 15.31 0.10 | 20 | I/II | mul |
| 053937.56-694525.4 | 4 | ··· ··· | ··· ··· | ··· ··· | ··· ··· | 18.11 0.12 | 17.38 0.16 | 15.68 0.11 | 10 | I | ext |
| 053938.09-694654.2 | 18 | 19.14 0.21 | 19.41 0.12 | 18.63 0.09 | 17.50 0.08 | ··· ··· | ··· ··· | ··· ··· | 0 | S in DR | |
| 053938.80-694436.0 | 38 | 13.82 0.09 | 14.54 0.05 | 14.61 0.17 | 13.89 0.09 | 13.70 0.06 | 13.54 0.09 | 13.29 0.06 | 0 | S | LMC X-1 |
| 053939.10-694443.7 | 34 | ··· ··· | ··· ··· | ··· ··· | ··· ··· | ··· ··· | ··· ··· | ··· ··· | 0 | D | |
| 053939.54-694400.2 | 19 | ··· ··· | ··· ··· | ··· ··· | ··· ··· | ··· ··· | ··· ··· | ··· ··· | 0 | D | |
| 053940.78-694632.0 | 14 | ··· ··· | ··· ··· | ··· ··· | ··· ··· | 16.80 0.07 | 16.66 0.06 | 15.55 0.10 | 10 | II | |
| 053941.89-694612.0 | 3 | ··· ··· | ··· ··· | ··· ··· | ··· ··· | 18.11 0.10 | ··· ··· | 13.31 0.10 | 20 | I/II | mul |
| 053943.74-694540.3 | 39 | ··· ··· | ··· ··· | ··· ··· | ··· ··· | 18.61 0.07 | 17.34 0.08 | 16.08 0.05 | 10 | III | mul |
| 053944.55-694436.2 | 21 | ··· ··· | ··· ··· | ··· ··· | ··· ··· | 16.61 0.03 | 15.86 0.03 | 15.33 0.03 | 10 | I/II | |
| 053945.18-694450.4 | 11 | 15.79 0.18 | 16.71 0.11 | 16.13 0.07 | 14.70 0.12 | 15.11 0.03 | 14.83 0.03 | 14.54 0.03 | 10 | III | ext |
| 053945.20-694508.1 | 22 | ··· ··· | ··· ··· | ··· ··· | ··· ··· | ··· ··· | ··· ··· | ··· ··· | 0 | D | |
| 053945.21-694533.1 | 41 | 15.44 0.05 | 16.45 0.04 | 16.02 0.04 | 15.66 0.06 | 15.53 0.07 | 15.25 0.10 | 15.45 0.23 | 0 | S in DR | |
| 053946.39-694435.5 | 20 | ··· ··· | ··· ··· | ··· ··· | ··· ··· | ··· ··· | ··· ··· | ··· ··· | 0 | D | |
| 053947.68-694526.1 | 16 | ··· ··· | ··· ··· | ··· ··· | ··· ··· | 17.90 0.06 | 17.71 0.09 | 17.28 0.13 | 10 | II | |
| 053948.25-694534.3 | 28 | ··· ··· | ··· ··· | ··· ··· | ··· ··· | ··· ··· | ··· ··· | ··· ··· | 0 | D | |
| 053948.83-694416.7 | 23 | ··· ··· | ··· ··· | ··· ··· | ··· ··· | ··· ··· | ··· ··· | ··· ··· | 0 | D peak | |
| 053949.26-694407.5 | 31 | ··· ··· | ··· ··· | ··· ··· | ··· ··· | ··· ··· | ··· ··· | ··· ··· | 0 | D | |
| 053950.29-694545.4 | 40 | ··· ··· | ··· ··· | ··· ··· | ··· ··· | ··· ··· | ··· ··· | ··· ··· | 0 | D | |
| 053952.39-694518.3 | 12 | ··· ··· | ··· ··· | ··· ··· | ··· ··· | ··· ··· | ··· ··· | ··· ··· | 0 | D | |
| 053952.60-694517.0 | 15 | ··· ··· | 15.15 0.08 | 14.82 0.09 | 14.07 0.15 | 14.11 0.02 | 13.91 0.02 | 13.78 0.01 | 10 | III | mul |
| 053956.62-694439.1 | 30 | ··· ··· | ··· ··· | ··· ··· | ··· ··· | ··· ··· | ··· ··· | ··· ··· | 0 | D | |
| 053956.92-695024.5 | 52 | ··· ··· | ··· ··· | ··· ··· | ··· ··· | 18.51 0.10 | 17.41 0.13 | 16.36 0.11 | 10 | II | mul |
| 053959.34-694526.3 | 5 | ··· ··· | ··· ··· | ··· ··· | ··· ··· | 16.34 0.03 | 14.00 0.02 | 11.96 0.02 | 10 | II | ext |
| 054000.69-694713.4 | 8 | 14.81 0.13 | 15.69 0.18 | 15.07 0.14 | 14.34 0.13 | 14.96 0.03 | 13.78 0.04 | 12.47 0.03 | 10 | III | ext |

Table 5—Continued

| Name (1) | No (2) | $U$ (3) | $B$ (4) | $V$ (5) | $I$ (6) | $J$ (7) | $H$ (8) | $K_s$ (9) | Flag (10) | Class. (11) | Remarks (12) |
|---|---|---|---|---|---|---|---|---|---|---|---|
| 054001.44-694801.6 | 44 | ··· ··· | ··· ··· | ··· ··· | ··· ··· | 18.51 0.08 | 17.43 0.09 | 16.60 0.09 | 10 | I/II | |
| 054003.49-694355.0 | 32 | ··· ··· | ··· ··· | ··· ··· | ··· ··· | 18.41 0.14 | 17.32 0.15 | 16.26 0.15 | 10 | YSC | |
| 054003.55-694710.0 | 42 | 18.36 0.24 | 18.86 0.09 | 17.51 0.09 | 16.21 0.07 | 15.49 0.02 | 14.88 0.01 | 14.70 0.02 | 10 | III | |
| 054004.13-694532.8 | 43 | ··· ··· | ··· ··· | ··· ··· | ··· ··· | ··· ··· | ··· ··· | ··· ··· | 0 | S in DR | |
| 054004.40-694437.6 | 1 | 16.90 0.20 | 14.67 0.12 | 15.55 0.14 | 13.94 0.14 | 14.18 0.04 | 13.99 0.05 | 13.53 0.11 | 10 | III | ext |
| 054005.91-694451.6 | 26 | ··· ··· | ··· ··· | ··· ··· | ··· ··· | ··· ··· | ··· ··· | ··· ··· | 0 | D | |
| 054006.85-694400.6 | 25 | ··· ··· | ··· ··· | ··· ··· | ··· ··· | ··· ··· | ··· ··· | ··· ··· | 0 | D | |
| 054008.53-694530.6 | 35 | ··· ··· | ··· ··· | ··· ··· | ··· ··· | ··· ··· | ··· ··· | ··· ··· | 0 | D | |
| 054009.49-694453.5 | 10 | ··· ··· | 21.92 0.31 | 20.76 0.22 | ··· ··· | 18.10 0.27 | 17.36 0.09 | 16.57 0.13 | 10 | I/II | mul |
| 054011.47-694504.5 | 13 | ··· ··· | ··· ··· | ··· ··· | ··· ··· | ··· ··· | ··· ··· | ··· ··· | 0 | D | |
| 054013.17-694948.8 | 45 | ··· ··· | ··· ··· | ··· ··· | ··· ··· | 18.72 0.08 | 17.50 0.08 | 16.20 0.04 | 10 | II | |
| 054014.04-694454.8 | 33 | ··· ··· | ··· ··· | ··· ··· | ··· ··· | 15.86 0.08 | 15.14 0.10 | 14.75 0.14 | 0 | S in DR | |
| 054019.00-694445.6 | 37 | ··· ··· | ··· ··· | ··· ··· | ··· ··· | ··· ··· | ··· ··· | 17.90 0.25 | 10 | II | ext |
| 054021.33-694944.0 | 36 | 19.55 0.10 | 19.77 0.05 | 19.27 0.06 | 18.26 0.09 | 17.97 0.09 | 16.69 0.12 | 16.66 0.16 | 10 | II | mul |
| 054037.09-694521.5 | 48 | ··· ··· | 21.16 0.12 | 19.66 0.09 | 17.84 0.08 | 16.43 0.13 | 15.55 0.14 | 14.70 0.12 | 0 | G | |
| 054044.66-694550.9 | 47 | ··· ··· | 21.02 0.12 | 20.41 0.11 | ··· ··· | 16.37 0.14 | 15.34 0.17 | 14.85 0.14 | 0 | G | |
| 054046.29-694441.1 | 50 | 20.64 0.22 | 18.95 0.04 | 17.54 0.05 | 15.93 0.05 | 14.82 0.05 | 13.93 0.05 | 13.79 0.06 | 0 | S in DR | |
| 054050.85-695001.9 | 46 | ··· ··· | ··· ··· | ··· ··· | ··· ··· | 18.21 0.08 | 17.05 0.06 | 15.86 0.04 | 10 | II | |

Note. — Column 1: source name. Column 2: Ranking of the brightness at 8 $\mu$m. Columns 3-9: $UBVIJHK_s$ photometric measurements in magnitudes. Measurements with uncertainties of 99.9 are the upper brightness limits as they include fluxes from neighbors or backgrounds. The uncertainties listed here are only errors in measurements and do not include errors in in flux calibration, i.e., 10% in $U$, 5% in $BV$, and 10% in $IJHK_s$. Thus, the total uncertainty of a flux is the quadratic sum of the measurement error and the calibration error. Column 10: data used for $JHK_s$ photometry: 0 – $JHK_s$ from 2MASS catalog, 10 – $JHK_s$ from IRSF data, 20 – $JK_s$ from VLT/NACO data. Column 11 and 12: classification and remarks: D – diffuse emission, DR – dusty region, ext – extended source, G – background galaxy, I/II/III – Type I/II/III YSO, mul – multiple, S – star, YSC – young star cluster.

Table 6. Inferred Physical Parameters from SED Fits to YSOs

| Source Name | [8.0] (mag) | Type | Stage Range | $\bar{M}_* \pm \Delta M_*$ ($M_\odot$) | $\bar{L}_{\rm tot} \pm \Delta L_{\rm tot}$ ($L_\odot$) | Physical Parameters of the Best-Fit Model | | | | | | |
|---|---|---|---|---|---|---|---|---|---|---|---|---|
| | | | | | | $M_*$ ($M_\odot$) | $R_*$ ($R_\odot$) | $T_*$ (K) | $M_{\rm env}$ ($M_\odot$/yr) | $M_{\rm disk}$ ($M_\odot$) | $A_V$ (mag) | $L_{\rm tot}$ ($L_\odot$) |
| 053937.56-694525.4 | 6.13 | I | 1.0 ± 0.0 | 34.8 ± 8.4 | 2.7E+05 ± 1.5E+05 | 29.3 | 270.2 | 7803 | 7.0E-04 | 0.0E+00 | 7.0 | 2.4E+05 |
| 053937.04-694536.7 | 6.60 | I | 1.0 ± 0.0 | 28.6 ± 5.5 | 1.2E+05 ± 5.1E+04 | 25.2 | 6.5 | 38000 | 1.5E-03 | 0.0E+00 | 0.0 | 8.2E+04 |
| 053935.99-694604.1 | 6.84 | I | 1.0 ± 0.0 | 18.5 ± 1.4 | 4.5E+04 ± 3.6E+02 | 17.3 | 10.4 | 26100 | 3.8E-03 | 0.0E+00 | 2.5 | 4.5E+04 |
| 053929.21-694719.0 | 7.20 | I | 1.0 ± 0.0 | 26.1 ± 1.5 | 8.8E+04 ± 2.5E+04 | 28.2 | 129.0 | 9549 | 7.1E-04 | 0.0E+00 | 2.3 | 1.2E+05 |
| 053937.53-694609.8 | 5.82 | I/II | 1.0 ± 0.0 | 31.2 ± 2.9 | 2.2E+05 ± 3.8E+04 | 29.3 | 270.0 | 7800 | 7.0E-04 | 0.0E+00 | 1.3 | 2.4E+05 |
| 053941.89-694612.0 | 5.93 | I/II | 1.0 ± 0.0 | 33.7 ± 2.6 | 1.7E+05 ± 2.9E+04 | 34.1 | 7.9 | 41760 | 2.5E-03 | 1.1E-01 | 12.7 | 1.7E+05 |
| 053944.55-694436.2 | 8.70 | I/II | 2.0 ··· | 12.2 ··· | 1.1E+04 ··· | 12.2 | 4.4 | 28500 | 1.5E-06 | 7.3E-03 | 0.9 | 1.1E+04 |
| 054001.44-694801.6 | 10.83 | I/II | 2.0 ± 0.0 | 6.4 ± 0.7 | 1.3E+03 ± 7.7E+02 | 6.3 | 3.1 | 19210 | 1.6E-07 | 1.2E-03 | 1.2 | 1.1E+03 |
| 053959.34-694526.3 | 6.54 | II | 1.0 ± 0.0 | 15.7 ± 2.3 | 3.0E+04 ± 9.7E+03 | 15.4 | 7.7 | 27940 | 1.1E-04 | 2.7E-02 | 0.6 | 3.2E+04 |
| 053940.78-694632.0 | 8.02 | II | 1.0 ± 0.0 | 9.4 ± 2.7 | 5.7E+03 ± 2.8E+03 | 7.9 | 8.8 | 15820 | 1.0E-05 | 6.0E-02 | 1.9 | 4.3E+03 |
| 053947.68-694526.1 | 8.14 | II | 1.7 ± 0.5 | 13.0 ± 2.4 | 1.4E+04 ± 8.4E+03 | 14.8 | 4.8 | 31100 | 0.0E+00 | 1.9E-01 | 0.0 | 2.0E+04 |
| 053933.86-694701.6 | 9.29 | II | 2.9 ± 0.5 | 12.3 ± 1.1 | 1.2E+04 ± 2.5E+03 | 12.9 | 4.5 | 29000 | 0.0E+00 | 7.1E-07 | 2.2 | 1.4E+04 |
| 054021.33-694944.0 | 9.65 | II | 2.0 ± 0.0 | 7.2 ± 0.1 | 1.9E+03 ± 6.5E+01 | 7.3 | 3.3 | 21120 | 0.0E+00 | 6.4E-04 | 2.2 | 2.0E+03 |
| 054019.00-694445.6 | 9.66 | II | 1.1 ± 0.2 | 10.8 ± 1.8 | 5.6E+03 ± 2.7E+03 | 11.2 | 32.1 | 8432 | 2.6E-04 | 6.4E-02 | 15.9 | 4.7E+03 |
| 054013.17-694948.8 | 10.96 | II | 1.9 ± 0.3 | 5.5 ± 0.6 | 7.1E+02 ± 1.6E+02 | 5.7 | 2.9 | 17860 | 0.0E+00 | 2.3E-02 | 2.8 | 7.6E+02 |
| 054050.85-695001.9 | 10.98 | II | 2.0 ± 0.0 | 5.6 ± 0.1 | 7.0E+02 ± 5.7E+01 | 5.7 | 2.9 | 17860 | 0.0E+00 | 2.3E-02 | 0.7 | 7.6E+02 |
| 053937.37-695120.8 | 11.33 | II | 1.3 ± 0.5 | 6.0 ± 0.2 | 5.1E+02 ± 5.9E+01 | 5.8 | 12.5 | 7098 | 3.1E-05 | 1.7E-01 | 0.8 | 4.7E+02 |
| 053956.92-695024.5 | 11.57 | II | 2.8 ± 0.4 | 7.7 ± 1.0 | 2.6E+03 ± 9.2E+02 | 8.2 | 3.5 | 22860 | 0.0E+00 | 4.9E-06 | 3.8 | 3.1E+03 |
| 054004.40-694437.6 | 5.40 | III | 1.0 ··· | 19.7 ··· | 5.3E+04 ··· | 19.7 | 23.3 | 18190 | 5.9E-03 | 0.0E+00 | 0.0 | 5.3E+04 |
| 054000.69-694713.4 | 6.89 | III | 2.5 ± 0.5 | 19.9 ± 2.6 | 4.7E+04 ± 1.5E+04 | 17.2 | 5.3 | 33000 | 1.3E-06 | 7.7E-05 | 0.0 | 3.1E+04 |
| 053945.18-694450.4 | 7.44 | III | 1.9 ± 0.3 | 16.6 ± 1.6 | 2.8E+04 ± 7.3E+03 | 16.6 | 5.2 | 32760 | 4.3E-07 | 2.3E-05 | 0.1 | 2.8E+04 |
| 054003.55-694710.0 | 10.34 | III | 1.0 ± 0.0 | 8.0 ± 0.5 | 1.2E+03 ± 3.1E+02 | 7.8 | 27.0 | 6700 | 3.8E-04 | 4.5E-03 | 1.8 | 1.3E+03 |
| 054009.49-694453.5 | 7.31 | mul(I/II) | 1.0 ± 0.0 | 20.8 ± 2.6 | 6.3E+04 ± 1.6E+04 | 22.7 | 18.0 | 23000 | 4.6E-03 | 0.0E+00 | 2.3 | 8.5E+04 |
| 053952.60-694517.0 | 8.14 | mul(III) | 1.0 ± 0.0 | 8.6 ± 0.7 | 2.4E+03 ± 3.8E+02 | 9.2 | 20.0 | 9200 | 9.6E-05 | 5.5E-01 | 0.1 | 2.8E+03 |
| 053930.01-694334.9 | 9.08 | mul(II) | 1.7 ± 0.5 | 7.7 ± 0.6 | 2.6E+03 ± 7.2E+02 | 7.5 | 3.4 | 22000 | 6.3E-05 | 1.6E-02 | 1.1 | 2.3E+03 |
| 054003.49-694355.0 | 9.48 | YSC | 1.8 ± 0.9 | 11.2 ± 1.8 | 8.4E+03 ± 3.9E+03 | 9.1 | 4.4 | 23000 | 2.1E-05 | 6.0E-04 | 3.4 | 5.0E+03 |
| 053943.74-694540.3 | 9.91 | mul(III) | 1.3 ± 0.6 | 9.4 ± 3.1 | 5.1E+03 ± 1.3E+04 | 9.0 | 16.0 | 11000 | 1.0E-03 | 1.7E-02 | 8.4 | 3.3E+03 |

Table 7. Inferred Physical Properties of YSOs in Tests of SED Fits

| Source Name | $\bar{M}_* \pm \Delta M_*$ ($M_\odot$) | $\bar{L}_{\rm tot} \pm \Delta L_{\rm tot}$ ($L_\odot$) | $\bar{\dot{M}}_{\rm env} \pm \Delta \dot{M}_{\rm env}$ ($M_\odot$/yr) | Stage Range | $\bar{M}_* \pm \Delta M_*$ ($M_\odot$) | $\bar{L}_{\rm tot} \pm \Delta L_{\rm tot}$ ($L_\odot$) | $\bar{\dot{M}}_{\rm env} \pm \Delta \dot{M}_{\rm env}$ ($M_\odot$/yr) | Stage Range |
|---|---|---|---|---|---|---|---|---|
| | Test on SED Fits to YSO with PAH Emission | | | | | | | |
| | Fits to Original SED | | | | Fits to PAH-corrected SED | | | |
| 053935.99−694604.1 | 18.5 ± 1.4 | 4.5E+04±3.6E+02 | 2.0E-03±2.2E-03 | 1.0±0.0 | 18.5 ± 3.6 | 4.1E+04±2.0E+04 | 1.6E-04±1.7E-04 | 1.0±0.0 |
| | Test on SED Fits to Multiple System with Sources at Similar Evolutionary Stages | | | | | | | |
| | Fits to SED w/ Integrated Fluxes | | | | Fits to SED of Component a | | | |
| 053941.89−694612.0 | 32.3 ± 2.9 | 1.6E+05±3.1E+04 | 1.3E-03±1.0E-03 | 1.0±0.0 | 26.9±2.5 | 1.0E+05±2.0E+04 | 1.1E-03±9.4E-04 | 1.0±0.0 |
| | | | | | Fits to SED of Component b | | | |
| | | | | | 24.8±2.5 | 8.2E+04±2.0E+04 | 8.5E-04±4.9E-04 | 1.0± 0.0 |
| | Test on SED Fits to Multiple System with Sources at Different Evolutionary Stages | | | | | | | |
| | Fits to SED w/ Integrated Fluxes | | | | Fits to SED w/ *HST UBVI* | | | |
| 054004.40−694437.6 | 19.7 ··· | 5.3E+04 ··· | 5.9E-03 ··· | 1.0 ··· | 20.5 ··· | 5.9E+04 ··· | 1.4E-04 ··· | 1.0 ··· |
| | | | | | Fits to mid-IR SED | | | |
| | | | | | 41.2±9.8 | 3.5E+05±1.8E+05 | 2.8E-03±2.0E-03 | 1.0±0.0 |

Table 8. Comparisons of Classifications of YSOs

| Name | [8.0] (mag) | Type | Stage Range | IRS Spec | Silicate Absorption | Other Classification[a] |
|---|---|---|---|---|---|---|
| 053937.56-694525.4 | 6.13 | I | 1.0 ± 0.0 | PE | √ | UCHII |
| 053937.04-694536.7 | 6.60 | I | 1.0 ± 0.0 | PE | √ | |
| 053935.99-694604.1 | 6.84 | I | 1.0 ± 0.0 | PE | × | HAeBe |
| 053929.21-694719.0 | 7.20 | I | 1.0 ± 0.0 | P | √ | maser |
| 053937.53-694609.8 | 5.82 | I/II | 1.0 ± 0.0 | PE | × | UCHII |
| 053941.89-694612.0 | 5.93 | I/II | 1.0 ± 0.0 | PE | √ | HAeBe |
| 054009.49-694453.5 | 7.31 | I/II(mul) | 1.0 ± 0.0 | PE | √ | |
| 053944.55-694436.2 | 8.70 | I/II | 2.0 ··· | | | |
| 054001.44-694801.6 | 10.83 | I/II | 2.0 ± 0.0 | | | |
| 053959.34-694526.3 | 6.54 | II | 1.0 ± 0.0 | PE | × | |
| 053940.78-694632.0 | 8.02 | II | 1.0 ± 0.0 | | | HAeBe |
| 053947.68-694526.1 | 8.14 | II | 1.7 ± 0.5 | | | |
| 053933.86-694701.6 | 9.29 | II | 2.9 ± 0.5 | | | HAeBe |
| 054021.33-694944.0 | 9.65 | II | 2.0 ± 0.0 | | | |
| 054019.00-694445.6 | 9.66 | II | 1.1 ± 0.2 | | | |
| 054013.17-694948.8 | 10.96 | II | 1.9 ± 0.3 | | | HAeBe |
| 054050.85-695001.9 | 10.98 | II | 2.0 ± 0.0 | | | HAeBe |
| 053937.37-695120.8 | 11.33 | II | 1.3 ± 0.5 | | | HAeBe |
| 053956.92-695024.5 | 11.57 | II | 2.8 ± 0.4 | | | |
| 054004.40-694437.6 | 5.40 | III | 1.0 ··· | PE | × | UCHII |
| 054000.69-694713.4 | 6.89 | III | 2.5 ± 0.5 | PE | × | HAeBe |
| 053945.18-694450.4 | 7.44 | III | 1.9 ± 0.3 | PE | × | |
| 053943.74-694540.3 | 9.91 | III(mul) | 1.3 ± 0.6 | | | HAeBe |
| 054003.55-694710.0 | 10.34 | III | 1.0 ± 0.0 | | | |

[a]Classifications of UCHII, HAeBe, and maser are from Indebetouw et al. (2004), Nakajima et al. (2005), and Lazendic et al. (2002).

Table 9. Physical Properties of YSOs with Maser and UCHIIs

| Maser/UCHII | YSO ID | Type | Stage Range | $M_\star$ ($M_\odot$) | Spec. Type | Spec.[a] Type | $\dot{M}_{\rm env}$ ($M_\odot$/yr) | $\dot{M}_{\rm crit}$[b] ($M_\odot$/yr) |
|---|---|---|---|---|---|---|---|---|
| maser | 053929.21−694719.0 | I | I | 26.1±1.5 | O7.5V | ··· | 5.1E-04±1.5E-04 | ··· |
| B0540−6946(1) | 054004.40−694437.6 | III | I | 19.7[c] | O9 V | O6 V | 5.9E-03 | 3.2E-05 |
| | | | I | 41.2±9.8[d] | O6 V | | 2.8E-03±2.0E-03 | |
| B0540−6946(4) | 053937.56−694525.4 | I | I | 34.8±8.4 | O6 V | O5.5 V | 2.3E-03±1.9E-03 | 6.8E-05 |
| B0540−6946(5) | 053937.53−694609.8 | I/II | I | 31.2 ± 2.9 | O7 V | O7.5 V | 2.2E-03±2.1E-03 | 4.1E-05 |

[a]The spectral type is determined from radio observations (Indebetouw et al. 2004).

[b]The critical infalling rate is adopted from Churchwell (2002).

[c]Parameters are inferred from model fits to the SED composed of all datapoints from $U$ to 70 $\mu$m.

[d]Parameters are inferred from model fits to the SED composed of *Spitzer* mid-IR datapoints.

Table 10. Physical and Star Formation Properties of GMCs in N 159 and N 44

| | N 159-E | N 159-W +N 159-2 | N 159-S +N 159-3 | N 44-C | N 44-S | N 44-N |
|---|---|---|---|---|---|---|
| $V_{\rm lsr}$ (km s$^{-1}$) | 234.1 | 236.1±2.4 | 233.0±1.6 | 282.5 | 279.4 | 283.8 |
| $\Delta V$ (km s$^{-1}$) | 7.6 | 5.7±0.3 | 7.7±0.8 | 7.2 | 15.8 | 3.8 |
| Size (pc) | 19.2 | 15.8± 1.0 | 19.5±2.4 | 86 | 136 | ··· |
| $M_{\rm vir}$ ($10^4 M_\odot$) | 17 | 16 | 36 | 37 | 210 | ··· |
| $M_{\rm lum}$ ($10^4 M_\odot$) | $21 \pm 13$ | $26 \pm 17$ | $39 \pm 25$ | $46 \pm 13$ | $145 \pm 41$ | ··· |
| $M_{\rm vir}/M_{\rm lum}$ | $0.8^{+1.3}_{-0.3}$ | $0.6^{+1.2}_{-0.2}$ | $0.9^{+1.7}_{-0.3}$ | $0.8^{+0.3}_{-0.2}$ | $1.4^{+0.6}_{-0.3}$ | ··· |
| $t_{\rm ff}$ (Myr) | 1.0 | 1.1 | 1.1 | 6.6 | 5.5 | ··· |
| $N_{\rm YSO}(M_{\rm u1} - M_{\rm u2})$[a] | 3(41-15) | 6(35-18) | 4(8-5) | 5(45-17) | 4(25-12) | 5(17-8) |
| $M^{\rm total}_{\rm YSO}(M_{\rm u} - M_{\rm l})$[b] ($M_\odot$) | $440^{+330}_{-150}$(41-1) | $1380^{+690}_{-290}$(35-1) | $200^{+220}_{-70}$(8-1) | $890^{+490}_{-30}$(45-1) | $475^{+70}_{-70}$(25-1) | $310^{+25}_{-40}$(17-1) |
| SFE$_{\rm YSO}$ | $2.6^{+2.0}_{-0.9}$E-3 | $8.6^{+4.3}_{-1.8}$E-3 | $5.6^{+6.1}_{-1.9}$E-4 | $2.4^{+1.3}_{-0.1}$E-3 | $2.3^{+0.3}_{-0.3}$E-4 | ··· |
| SFR$_{\rm YSO}$ ($M_\odot$ yr$^{-1}$) | $4.4^{+3.3}_{-1.5}$E-4 | $1.4^{+0.7}_{-0.3}$E-3 | $2.0^{+2.2}_{-0.7}$E-4 | $8.9^{+4.9}_{-0.3}$E-4 | $4.8^{+0.7}_{-0.7}$E-4 | $3.1^{+0.3}_{-0.4}$E-4 |
| $\epsilon_{\rm ff}$ | $2.6^{+2.0}_{-0.9}$E-3 | $8.6^{+4.3}_{-1.8}$E-3 | $5.6^{+6.1}_{-1.9}$E-4 | $1.6^{+0.5}_{-0.2}$E-2 | $1.2^{+0.2}_{-0.2}$E-4 | ··· |
| $L({\rm H}\alpha)_{\rm obs}$ ($\times 10^{37}$ ergs s$^{-1}$) | 8.9±0.9 | 4.0±0.4 | 0.16±0.02 | 160±20 | 110±10 | 0.49±0.05 |
| $L(24\ \mu{\rm m})$ ($\times 10^{38}$ ergs s$^{-1}$) | 46±5 | 28±3 | 0.55±0.06 | 23±2 | 14±1 | 1.8±0.2 |
| Aperture Radius ($''$) | 110 | 90 | 120 | 140 | 270 | 180 |
| SFR$_{H\alpha+24}$ ($M_\odot$ yr$^{-1}$) | 1.20±0.16E-3 | 6.57±0.96E-4 | 1.72±0.21E-5 | 1.21±0.11E-3 | 8.06±0.75E-4 | 5.46±0.65E-5 |
| $\Sigma_{\rm H_2}$ ($M_\odot$ pc$^{-2}$) | 35 | 62 | 62 | 59 | 42 | 25 |
| $\Sigma_{\rm HI}$ ($M_\odot$ pc$^{-2}$) | 90 | 99 | 117 | 54 | 72 | 45 |
| SFR$_{H\alpha+24}$ ($M_\odot$ yr$^{-1}$ kpc$^{-2}$) | 0.54±0.07 | 0.44±0.07 | 6.4±0.8E-3 | 0.33±0.04 | 0.060±0.005 | 9.1±1.1E-3 |
| SFR$_{\rm YSO}$ ($M_\odot$ yr$^{-1}$ kpc$^{-2}$) | $0.20^{+0.15}_{-0.07}$ | $0.92^{+0.41}_{-0.19}$ | $0.075^{+0.083}_{-0.026}$ | $0.24^{+0.13}_{-0.01}$ | $0.035^{+0.005}_{-0.005}$ | $0.051^{+0.004}_{-0.007}$ |
| SFR$_\Sigma$ ($M_\odot$ yr$^{-1}$ kpc$^{-2}$) | 0.22 | 0.32 | 0.36 | 0.19 | 0.19 | 0.10 |

[a]Number of YSOs with $\bar{M}_*$ in the mass range (u1-u2).

[b]Total mass of YSOs extrapolated for the mass range (u-l).

This figure "f2.jpg" is available in "jpg"  format from:

http://arxiv.org/ps/1007.5326v1

This figure "f4.jpg" is available in "jpg"  format from:

http://arxiv.org/ps/1007.5326v1

This figure "f8.jpg" is available in "jpg"  format from:

http://arxiv.org/ps/1007.5326v1

This figure "f10.jpg" is available in "jpg"  format from:

http://arxiv.org/ps/1007.5326v1